HHS Public Access

Author manuscript

FEBS J. Author manuscript; available in PMC 2019 February 01.

Published in final edited form as:

FEBS J. 2018 February ; 285(3): 481–500. doi:10.1111/febs.14367.

Impaired muscle relaxation and mitochondrial fission associated with genetic ablation of cytoplasmic actin isoforms

Allison R. O'Rourke[1], **Angus Lindsay**[2], **Michael D. Tarpey**[3], **Samantha Yuen**[4], **Preston McCourt**[4], **D'anna M. Nelson**[4], **Benjamin J. Perrin**[5], **David D. Thomas**[4], **Espen E. Spangenburg**[3], **Dawn A. Lowe**[2], and **James M. Ervasti**[4]

[1]Department of Genetics, Cell Biology and Development University of Minnesota, Minneapolis, MN, 55455

[2]Department of Rehabilitation Medicine, University of Minnesota, Minneapolis, MN, 55455

[3]East Carolina Diabetes and Obesity Institute, Department of Physiology, East Carolina University, Greenville, NC, 27858

[4]Department of Biochemistry, Molecular Biology, and Biophysics University of Minnesota, Minneapolis, MN, 55455

[5]Department of Biology Indiana University-Purdue University Indianapolis, Indianapolis, Indiana, 46022

Abstract

While α_{sk}-actin isoforms predominate in adult striated muscle, skeletal muscle-specific knockouts of non-muscle cytoplasmic β_{cyto}- or γ_{cyto}-actin each cause a mild, but progressive myopathy affected by an unknown mechanism. Using transmission electron microscopy, we identified morphological abnormalities in both the mitochondria and the sarcoplasmic reticulum in aged muscle-specific β_{cyto}- and γ_{cyto}-actin knockout mice. We found β_{cyto}- and γ_{cyto}-actin proteins to be enriched in isolated mitochondrial associated membrane preparations, which represent the interface between mitochondria and sarco-endoplasmic reticulum important in signaling and mitochondrial dynamics. We also measured significantly elongated and interconnected mitochondrial morphologies associated with a significant decrease in mitochondrial fission events in primary mouse embryonic fibroblasts lacking β_{cyto}- and/or γ_{cyto}-actin. Interestingly, mitochondrial respiration in muscle was not measurably affected as oxygen consumption was

Send correspondence to: jervasti@umn.edu.

Author Contributions:

Allison R. O'Rourke (Conception and design, Acquisition of Data, Analysis of Data, Figure Preparation, Drafting of Manuscript, Editing)
Angus Lindsey (Conception and design, Acquisition of Data, Editing)
Michael D. Tarpey (Conception and design, Acquisition of Data, Editing)
Samantha Yuen (Conception and design, Acquisition of Data, Editing)
Preston McCourt (Conception and design, Acquisition of Data, Editing)
D'anna Nelson (Conception and design, Acquisition of Data, Editing)Benjamin J. Perrin (Conception and design, Editing)
David D. Thomas (Conception and design, Editing, Supervision)
Espen E. Spangenberg (Conception and design, Editing, Supervision)
Dawn A. Lowe (Conception and design, Editing, Supervision)
James M. Ervasti (Conception and design, Drafting of Manuscript, Editing, Supervision)

similar in skeletal muscle fibers from 12 month-old muscle-specific β_{cyto}- and γ_{cyto}-actin knockout mice. Instead, we found that the maximal rate of relaxation after isometric contraction was significantly slowed in muscles of 12 month-old β_{cyto}- and γ_{cyto}-actin muscle-specific knockout mice. Our data suggest that impaired Ca^{2+} re-uptake may presage development of the observed SR morphological changes in aged mice while providing a potential pathological mechanism for the observed myopathy.

Graphical Abstract

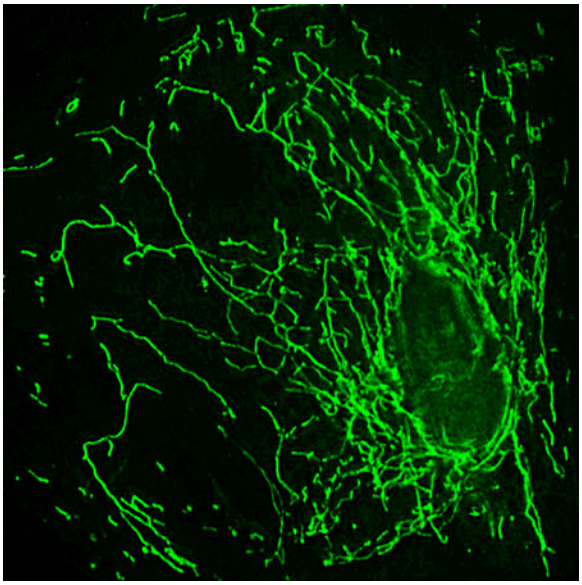

Gene knockout of either cytoplasmic actin isoform (βcyto- or γcyto-actin) results in elongated mitochondrial morphology and decreased mitochondrial fission in mouse embryonic fibroblasts. Ablation of either βcyto- or γcyto-actin in skeletal muscle also results in altered mitochondrial and sarcoplasmic reticulum morphologies in aged skeletal muscle, as well as impaired skeletal muscle relaxation.

Keywords

β-actin; γ-actin; isoforms; mitochondrial dynamics

Introduction

While abundantly expressed skeletal (α_{sk}-actin) and cardiac (α_{ca}-actin) actins are essential constituents of sarcomeric thin filaments in adult striated muscle [1,2], non-muscle cytoplasmic actins (β_{cyto}- and γ_{cyto}-actin) are the predominant isoforms in myoblasts [3,4] and have been implicated in several key steps of myogenesis during development [5–8]. After myogenesis, very low levels of β_{cyto}- and γ_{cyto}-actin remain in adult skeletal muscle and localize to an extra-sarcomeric cytoskeleton that includes the subsarcolemmal costamere [9–12], regions of the sarcoplasmic reticulum (SR) flanking the Z-disk, and mitochondria [9,13–16].

Several studies have shown that γ_{cyto}-actin colocalizes with isoforms of ankyrin, tropomyosin and tropomodulin at the extra-sarcomeric cytoskeleton [13,14,17,18]. Knockout of the tropomyosin isoform TM5NM1 [19], or disruption of tropomodulin 3 (Tmod3) localization as a result of tropomodulin 1 (Tmod1) knockout [20] both perturb the peri-Z-disk elements with associated defects in triad morphology and excitation-contraction coupling. Knockdown of clathrin heavy chain was shown to drive γ_{cyto}-actin displacement from the sarcolemma and loss of contractile force presumably due to uncoupling of myofibrils from costameres [21]. A recent proteomic study reported that γ_{cyto}-actin was found in an isolated complex containing four-and-a-half LIM domain protein 1 (FHL1) protein [22], while gene knockout of FHL1 causes a progressive skeletal myopathy associated with sarcoplasmic reticulum and mitochondrial disorganization in mice [23]. Collectively, these studies suggest that extra-sarcomeric cytoplasmic actins contribute to the function of several organelles in adult skeletal muscle.

To more directly test the functional importance of non-muscle cytoplasmic actins in skeletal muscle, we previously generated muscle-specific knockout mice lacking either γ_{cyto}-actin (*Actg1*-msKO, Sonnemann *et al.*, 2006), or β_{cyto}-actin (*Actb*-msKO, Prins *et al.*, 2011). These two single gene knockouts developed qualitatively similar phenotypes characterized by a progressive myopathy with significant myofiber degeneration/regeneration and muscle weakness, but without any detectable perturbations of the costameric lattice or intracellular organelles in mice 3–6 months old [12,24]. Notably, ultrastructural defects in the sarcoplasmic reticulum of Tmod1 knockout mice were not apparent until 6 months of age [14,20]. The progressive nature of both Actg1-msKO and Actb-msKO suggests that partial functional redundancy of β_{cyto}- and γ_{cyto}-actins may slow the development of the phenotypes observed after knockout of other actin-associated proteins in the extra-sarcomeric cytoskeleton [14,20].

Here, we examined muscle ultrastructure as a function of age using transmission electron microscopy (TEM) and show that skeletal muscles from 22–25 month old Actg1-msKO and Actb-msKO mice exhibit misshaped mitochondria and dilated and vesiculated sarcoplasmic reticulum compared to age-matched control animals (Actg1-msCT and Actb-msCT mice), or younger knockout animals. We also demonstrate that both β_{cyto}- and γ_{cyto}-actin co-enrich with biochemically isolated mitochondrial-associated membrane fractions. While mouse primary embryonic fibroblasts ablated for β_{cyto}- and/or γ_{cyto}-actin exhibited markedly increased mitochondrial lengths and decreased rates of fission, no significant deficit in mitochondrial respiration, oxygen consumption, or ROS was measured in isolated Actg1-msKO or Actb-msKO skeletal muscle fiber bundles or intact Actb-msKO mice. Finally, we measured a small but significant decrease in the maximal relaxation rate in extensor digitorum longus (EDL) muscles of Actg1-msKO and Actb-msKO mice which was not linked to a defect in SERCA function. Collectively, our present data are consistent with previous studies [20,23,25–27], and extend them by showing that specific loss of either β_{cyto}- or γ_{cyto}-actin from mouse embryonic fibroblasts causes a defect in mitochondrial fission while their loss from the extra-sarcomeric cytoskeleton of skeletal muscle mildly perturbs sarcoplasmic reticulum physiological function.

Results

Altered Sarcoplasmic Reticulum and Mitochondrial Morphologies in Aged Cytoplasmic Actin KO Skeletal Muscle

Several other groups have observed age-dependent morphological defects in sarcoplasmic reticulum and mitochondria after genetic ablation of actin binding proteins associated with the extra-sarcomeric actin cytoskeleton [14,20,23]. Therefore, we utilized TEM to examine the muscle ultrastructure from Actg1-msKO and Actb-msKO animals at 6, 12, and 22–25 months of age (Figure 1). Consistent with our previous studies [12,24], analysis of longitudinal sections from 6 month-old animals showed muscle architecture, including Z-disk alignment that was not different from age-matched Actg1-msCT or Actb-msCT control mice (Figure 1 A–C, P; Figure 2A). While muscles from most 12 month-old animals were also not different from Actg1-msCT or Actb-msCT (denoted with a white arrowhead in Figure 1D, F, P), one Actg1-msKO sample displayed dilation of the sarcoplasmic reticulum (denoted with a white arrow in Figure 1 E, P). At 22–25 months of age, all Actg1-msKO and Actb-msKO muscles displayed normal Z-disk alignment, but presented with sarcoplasmic reticulum dilation (Figure 1 G–I, M; Figure 2 B). TEM examination of skeletal muscle in cross section revealed abnormal mitochondrial morphology in Actg1-msKO and Actb-msKO muscles at 22–25 months of age (Figure 1 J–L, Q). Actg1-msKO and Actb-msKO muscle exhibited a subset of mitochondria which appeared rounded in the two-dimensional images (white arrows, Figure 1 K, L) in comparison to the more prevalent elongated mitochondria observed in age-matched Actg1-msCT or Actb-msCT muscle (white arrow heads, Figure 1 J–L). The measured mitochondrial length to width ratios confirmed the qualitative observation (Figure 1 Q). Although these measurements were made on two-dimensional images and mitochondria are three-dimensional structures, the observed change in the length to width ratio in cross section, is suggestive of an overall change in mitochondrial morphology. Higher magnification images reveal internal mitochondrial morphology which is unchanged between control and knockout samples (Figure 1 M–O). Mitochondrial electron density and cristae morphology appear to be maintained in knockout muscle. Another cytoskeletal protein, the intermediate filament desmin is known to be important for proper mitochondrial morphology [28,29]. However the observed mitochondrial phenotype in Actg1-msKO and Actb-msKO is likely not impacted by changes in desmin, which was expressed at similar levels (Figure 3 A–B) and localization (Figure 3 C–E) relative to control muscle. Consistent with other studies [14,20,23], our TEM data reveal age-dependent ultrastructural defects in the sarcoplasmic reticulum and mitochondria of Actg1-msKO and Actb-msKO muscles, but which take longer to manifest than previously observed with genetic ablation of Tmod1 or FHL1 [14,20,23].

Morphological defects in both the sarcoplasmic reticulum and mitochondria of Actg1-msKO and Actb-msKO muscles suggested that β_{cyto}- and γ_{cyto}-actin may interact with both organelles at their site of close apposition. Mitochondrial associated membranes (MAMs) are a functionally important interface between mitochondria and the sarco-/endo-plasmic reticulum involved in mitochondrial respiration, Ca^{2+} crosstalk, cell death signaling, lipid metabolism, and mitochondrial dynamics [30–34]. Therefore, we biochemically isolated MAM, mitochondrial, and endoplasmic reticulum fractions from wildtype mouse liver [35]

and performed western blot analysis to identify the fractions containing β_{cyto}- and γ_{cyto}-actin immunoreactivity using previously established antibodies specific to each isoform (Figure 4) [24,12,36,37]. As expected, both γ_{cyto}- and β_{cyto}-actin were present in the cytosolic fraction (verified by tubulin immunoreactivity), weakly present in the crude mitochondrial fraction (identified by cytochrome C), and most enriched in the isolated MAM fraction verified by the presence of FACL4, a lipid enzyme localized to the MAM [38,39]. Thus, both β_{cyto}- and γ_{cyto}-actin co-enrich with a membrane fraction thought to represent the interface between the sarcoplasmic reticulum and mitochondria, which each display age-dependent perturbations in morphology when β_{cyto}- or γ_{cyto}-actin are knocked out (Figure 1).

Perturbation of Mitochondrial Dynamics in Cytoplasmic Actin-Null Mouse Embryonic Fibroblasts

Abnormalities in mitochondrial morphology imply a defect in mitochondrial dynamics controlled by the opposing processes of fission and fusion [40]. Both the endoplasmic reticulum and actin have recently been shown to play key roles in mitochondrial fission in many cell types [25,26,41], however, mitochondrial dynamics are challenging to measure in adult skeletal muscle fibers [42]. Therefore, we imaged mitochondria in primary mouse embryonic fibroblasts (MEFs) homozygous for floxed Actb or Actg1 alleles which were treated with adenovirus-5 CRE to knockout the target gene or adenovirus-5 GFP as a control [36]. MEFs ablated for either β_{cyto}-actin, γ_{cyto}-actin, or both actins displayed individual mitochondria which were significantly larger by surface area compared to mitochondrial size in control MEFs (Figure 5 A–G). Mitochondria in Actg1, Actb, and Actb/Actg1 KO MEFs compared to control (Actg1-CT or Actb-CT) MEFs have similar numbers of individual mitochondria, or mitochondria without branches (Figure 5 H) as measured using the Fiji plug-in MiDA [43]. However, MEFs lacking either β_{cyto}-actin or γ_{cyto}-actin have an increase in network or branched mitochondria (Figure 5 I). While the number of mitochondria with branches (Figure 5 I) is greater in knockout MEFs compared to controls, the length of the branches (Figure 5 J) and the number of branches per network (Figure 5 K) is not different. The most likely explanations for the measured increase in mitochondrial size or network formation would be a decrease in the rate of mitochondrial fission, or an increase in mitochondrial fusion. Therefore, mitochondria were live-imaged and the frequencies of fission and fusion events were quantified. While the frequency of fusion events was not different across all MEF pools analyzed (Figure 5 I), the frequency of fission events were significantly decreased in Actg1, Actb, and Actb/Actg1 KO MEFs compared to control (Actg1-CT or Actb-CT) MEFs (Figure 5 J). The observed decrease in fission could be linked to a decrease in the abundance of proteins known to be critical for mitochondrial dynamics however, we found that proteins involved in mitochondrial fission, mitochondrial fission 1 (Fis1; Figure 6 A–B) or fusion, mitofusin2 (MFN2) and dominant optic atrophy1 (OPA1; Figure 6 C–F) were not depleted in Actg1-msKO or Actb-msKO muscle relative to controls. Our results are consistent with the previously defined role for actin in mitochondrial fission [25,26] and extend previous studies by demonstrating that both β_{cyto}- and γ_{cyto}-actin isoforms non-redundantly support mitochondrial fission.

Normal Mitochondrial Respiration in Cytoplasmic Actin KO Skeletal Muscle

Because perturbations in mitochondrial shape, dynamics, and function are often interlinked [44–46], we investigated whether mitochondrial respiration was altered in muscle fiber bundles from the red portion of the gastrocnemius muscle from 12 month-old Actg1-msKO and Actb-msKO mice. No change was detected in the abundance of protein components of electron transport chain (ETC) complexes I–IV (Figure 7), which correspond to no measureable differences in respiratory function. Specifically, no differences were detected in Complex I Leak or ADP-stimulated Complex I or Complex I and II respiration between fiber bundles isolated from age-matched Actg1-msKO and Actg1-msCT, or Actb-msKO and Actb-msCT animals (Figure 8 A–C). Nor were differences detected in Complex II or IV-mediated respiration (Figure 8 D–E). Complex I control and succinate control: the portion of respiration attributed to complex I or complex II, respectively, via the Q-junction (Figure 8 F–G), respiratory control ratio (RCR) and coupling efficiency: indicators of mitochondrial coupling (Figure 8 H–I), E-Super-C; a measure of incomplete channeling of electrons through the Q-junction during Complex I and II respiration (Figure 8 J) were also not different among fiber bundles from each group. Taken together these data indicate that the absence of either β_{cyto}-actin or γ_{cyto}-actin does not lead to perturbations in mitochondrial respiration at 12 months.

As defects in mitochondrial morphology were most evident in aged Actg1-msKO and Actb-msKO muscles (Figure 1 J–L, Q), we also measured whole body energy expenditure in 22–25 month-old Actb-msCT and Actb-msKO mice (Figure 9). Consistent with our measurements of oxygen consumption in isolated gastrocnemius muscles (Figure 8) and primary mouse embryonic fibroblasts [36], there was no difference between aged Actb-msCT and Actb-msKO mice in any measured parameter of whole body respiratory function (Figure 9).

Though respiration wasn't detectibly perturbed in Actg1-msKO or Actb-msKO muscle, another aspect of mitochondria function which could be affected is the emission of reactive oxygen species (ROS). Examination of the ROS species H_2O_2 in isolated skeletal muscle fibers indicated that buffered and non-buffered H_2O_2 emission is not significantly different in knockout muscle compared to controls (Figure 10 A). The scavenger index, which is the percent increase of non-buffered over buffered H_2O_2 production, is also similar in control and knockout muscle (Figure 10 B). These results indicate that the alterations in mitochondrial morphology and dynamics caused by genetic ablation of Actg1 or Actb (Figures 1, 3) are not associated with a measurable impairment in mitochondrial function.

Impaired Relaxation in Cytoplasmic Actin KO Skeletal Muscle

In the absence of a measurable deficit in mitochondrial function (Figure 8, Figure 9) to explain the mild, but progressive myopathy caused by muscle-specific ablation of Actb or Actg1 [12,24], we characterized contractile function of isolated EDL muscles from 12 month-old Actg1-msCT and Actg1-msKO animals, and 12 and 22–25 month-old Actb-msCT and Actb-msKO mice. Further analysis of tetanic isometric contractions showed that specific force, maximal rate of contraction, force development time, loss of force during a fatigue protocol as well as recovery of force following a submaximal fatigue protocol were

not different (Table 1, Figure 11 A–C), indicating that the ability of Actg1-msKO and Actb-msKO muscles to respond to electrical stimuli, release Ca^{2+}, and produce force [47–49] were largely unaffected. Interestingly, the maximal rate of relaxation was significantly slowed in 12 month-old Actg1-msKO and Actb-msKO muscles compared to age matched Actg1-msCT and Actb-msCT muscles, as was ½ relaxation time in the Actg1-msKO (Table 1, Figure 11 D). By 22–25 months of age, the maximal rate of relaxation in Actb-msCT muscles slowed to the point that it was no longer significantly different from Actb-msKO muscles (Table 1, Figure 11 D).

While Ca^{2+} reuptake by the sarco-/endo-plasmic reticulum Ca^{2+}-ATPase (SERCA) is primarily responsible for muscle relaxation rate [48,50], western blot analysis revealed similar levels of immunoreactivity in Actg1-msKO compared to Actg1-msCT, and in Actb-msKO compared to Actb-msCT skeletal muscle lysates against the primary isoform of SERCA expressed in skeletal muscle and a regulator of SERCA, small Ankyrin 1 (Figure 12 A–C) [51]. Calsequestrin also did not show any detectible change in abundance between Actg1-msKO or Actb-msKO and control SR (Figure 12 D–E), suggesting that the SR phenotype we observe by TEM (Figure 1 G–I, M; Figure 2 B) is likely due to SR dilation rather than SR proliferation. The similar levels of SERCA1a as well as small Ankyrin 1 in control and knockout samples indicate that it is unlikely to be a deficit in SERCA availability or activation that causes the observed phenotype. We also measured SERCA ATPase activity in SR isolated from control and knockout muscle in the presence or absence of inhibitors. We found no significant differences in SERCA activity between Actb-msKO (Figure 13 A–B) and controls. Dysregulation of Ca^{2+} can result in the activation of the unfolded protein response (UPR) as a result of cellular stress [52–55]. However, we observed no change in the abundance of several UPR proteins in Actg1 and Actb KO skeletal muscle (Figure 14). None-the-less, the dilated sarcoplasmic reticulum (Figure 1) and slowed relaxation (Table 1, Figure 11) both suggest that sarcoplasmic Ca^{2+} regulation is impaired in Actg1-msKO and Actb-msKO skeletal muscles.

Discussion

Though only accounting for a minute fraction of the total actin pool in adult skeletal muscle [56], non-muscle cytoplasmic γ_{cyto}- and β_{cyto}- actin isoforms have been shown to localize to a diverse array of cellular structures in skeletal muscle. Some structures to which cytoplasmic actin has been localized in adult skeletal muscle include subsarcolemmal costameres [9–12], mitochondria [9] and the peri-Z-disk region where SR localizes [13–16]. However, it is still unclear how ablation of γ_{cyto}- or β_{cyto}-actin in skeletal muscle causes a mild, but progressive myopathy [12,24]. Here we show that knockout of γ_{cyto}- or β_{cyto}- actin causes perturbation in both mitochondrial morphology and fission, supporting a link between γ_{cyto}- or β_{cyto}- actin localization at the mitochondria and a functional role in mitochondrial dynamics.

Dynamic mitochondria in skeletal muscle are critical for maintaining bioenergetics [57,58]. As a consequence of the high energy demand of skeletal muscle, perturbations in multiple aspects of mitochondrial dynamics can be fatal in mice [46,59]. Mitochondria are distributed in skeletal muscle to enable maximal functional connectivity with surrounding structures

[30,60,61] including other mitochondria [62] with which they regularly undergo fusion [57]. In non-muscle cells, both actin and the endoplasmic reticulum have been implicated in the fission process [25,26,63]. Because mitochondrial dynamics are critical in all cell types and occur with higher frequency in non-muscle cells, we utilized a MEF model to study dynamics and found decreased fission in γ_{cyto}-, β_{cyto}-, and double actin KO MEFs, indicating that γ_{cyto}- and β_{cyto}- actin isoforms are individually important for mitochondrial fission.

The observed alterations in mitochondria morphology and measured changes in mitochondrial dynamics were not paired with detectable differences in mitochondrial respiration or an alteration in redox balance, specifically reactive oxygen species (ROS) emission. This finding supports the idea in the mitochondrial dynamics field that elongated mitochondria may act as a protective feature.

At the mitochondrial-SR/ER interface, Ca^{2+} signaling can influence mitochondria respiration rates and even initiate cell death [60,64–66]. Here, we demonstrate enrichment of both γ_{cyto}- and β_{cyto}- actin with the MAM. The MAM forms a small microenvironment which is important for a large array of functions in addition to Ca^{2+} signaling, including but not limited to: mitochondrial fission, ER stress, ROS signaling, and lipogenesis [25,26,61,67–72]. We observed alterations in the morphology of both organelles which form the MAM. Dysregulation of the signaling cascades can be caused by structural malformations of the MAM [73–75]. Therefore, loss of γ_{cyto}- or β_{cyto}- actin from the mitochondrial-SR/ER interface may impair inter-organelle signaling.

Ca^{2+} signaling is critical to regulating skeletal muscle contraction and relaxation. Problems with Ca^{2+} sequestration can occur at a number of points including: leak through the RYR, SERCA, the membrane, or ryanodine receptor or SERCA dysfunction. However we did not observe changes in the abundance or activity of SERCA (Figure 12 and Figure 13) suggesting that Ca^{2+} leak through RYR or the dilated SR membrane may be the cause of the observed perturbations in relaxation rate. Swelling of the SR, similar to what we observed here, has been seen alongside defective skeletal muscle Ca^{2+} release [20], supporting a role for Ca^{2+} in the γ_{cyto}- and β_{cyto}- actin skeletal muscle KO relaxation defect. Cellular stressors can induce Ca^{2+} dysregulation (Ermak and Davies, 2002). One such stress is muscle aging, or sarcopenia, which has been linked to alterations in Ca^{2+} flow [76]. Oxidation of the RYR with aging leads to SR Ca^{2+} leak, further ROS elevation and ultimately loss of muscle [76]. The decreased relaxation rate seen here in 12 month old Actg1-msKO and Actb-msKO skeletal muscle preceded a similar decrease in Actb-msCT skeletal muscle at 22–25 months of age (Figure 11D), suggesting that knockout of either cytoplasmic actin may accelerate aging in skeletal muscle.

The partial redundancy of the cytoplasmic actin isoforms, illustrated by the similar but modest phenotypes displayed when either are knocked-out, indicates that both are important but can likely compensate in some aspects for the other. An explanation for this partial overlap is likely that the sequences of γ_{cyto}- and β_{cyto}- actin are highly conserved and differ only by the 3'UTR sequences and 4 biochemically similar amino acid changes [77,78]. Despite the high degree of sequence identity, γ_{cyto}- and β_{cyto}- actin have differing

polymerization dynamics and modifications [77,79,80]. The presence of the phenotypes observed here suggests that each isoform does play a unique and vital role in the actin cytoskeleton.

Methods

Mouse Lines

Mice (*Mus musculus*) containing the conditional floxed *Actb* [81] and *Actg1* [24] alleles as described previously were each backcrossed on to the C57BL/6 background for a minimum of five generations. To generate knockout mice, each line was crossed to mice expressing cre-recombinase under the skeletal muscle specific human skeletal actin promoter (HSA-Cre mice were provided by Judith Melki, INSERM, Evry, France; Miniou et al., 1999). Knockout animals were homozygous for either the Actb or Actg1 floxed alleles, and hemizygous for HSA-cre, controls were age-matched floxed mice lacking HSA-cre that are referred to as either Actb-msCT or Actg1-msCT. All mice examined were male. Standard PCR analysis was used to confirm genotype. All animals were cared for according to the University of Minnesota Institutional Animal Care and Use Committee policy.

Muscle Fiber Imaging

Extensor digitorum longus (EDL) muscles were harvested from 13–14 month old perfusion-fixed mice and immunostained for desmin (D93F5; Cell Signaling Technology, Danvers, MA, USA). Perfusion media (50 mM Pipes, 5 mM EGTA, 2 mM MgSO4, 10% (vol/vol) DMSO, and 0.1% Triton X-100, pH 6.8) contains 4% (wt/vol) paraformaldehyde. Muscles were further postfixed in 4% (wt/vol) paraformaldehyde in PBS (PBS: 8 mM NaH2PO4, 42 mM Na2HPO4, and 150 mM NaCl, pH 7.5) for 24 hours while rotating. Single muscle fibers were mechanically teased apart and incubated with anti-desmin overnight with rotation. Goat anti-rabbit secondary antibody coupled to Alexa Fluor 488 was used for visualization. Fibers were mounted on slides using Prolong Gold antifade reagent with DAPI (Cell Signaling Technology, Danvers, MA, USA) to visualize nuclei. Fibers were imaged on the Olympus FluoView FV1000 with the 60× oil immersion objective using the accompanying software. ImageJ sum slices projection was used to combine two Z-stacks for a total 0.8 microns depth. Brightness and contrast were adjusted using ImageJ [83]. Images are representative of n = 2 mice per genotype and n = 10 fibers per mouse.

Cell Culture and Imaging

Primary MEFs were cultured from E13.5 $Actb^{L/L}$, $Actg1^{L/L}$ and double $Actb^{L/L}/Actg1^{L/L}$ mouse embryos as described previously [36,84]. Briefly: MEFs from individual embryos were cultured at 37°C in 5.0 % CO_2 in DMEM media (supplemented with 10% FBS, 1% Pen/Strep, 0.5ug/mL Fungizone; Invitrogen Carlsbad, CA, USA), counted, and split into two pools. One pool was treated with the control adenovirus Ad5-GFP (Ad5CMV-hrGFP) the other group was treated with Ad5-Cre (Ad5CMV-Cre-eGFP) virus purchased from The University of Iowa Viral Vector Core (Iowa City, IA, USA) explicitly following the Core's Adenovirus Adfection protocol (http://www.medicine.uiowa.edu/vectorcore).

On the seventh ($Actb^{L/L}$, $Actg1^{L/L}$ MEFs) or ninth ($Actb^{L/L}$/$Actg1^{L/L}$ MEFs) day post infection cells showed complete knockout of protein by western blot as previously published [36]. Once knockout was confirmed by western blot, MEFs were stained with 0.01nM MitoTracker CMXRos (ThermoFisher Scientific M7512; Waltham, MA, USA) in Opti-MEM with 10%FBS for 15 min. Media was replaced and cells were imaged using a GE Applied Precision DeltaVision Deconvolution Microscopy system (Little Chalfont, Buckinghamshire, UK) with a 60x numerical aperture 1.42 objective and Photometrics Coolsnap HQ camera (Tucson, AZ, USA). Using a z-stacked image Imaris Imaging software by Bitplane (Belfast, Northern Ireland, UK) was used to define individual mitochondria (overlapping mitochondria were excluded from this analysis) and determine the surface area of all individual mitochondrion. To assess the overlapping mitochondria and network formation the Mitochondria Network Analysis (MiNA) toolset plugin for Fiji was used[43,83]. Briefly, MiNA defined the mitochondrial network and converted it to binary, then a mitochondrial skeleton was defined, this skeleton was then assessed for the number of mitochondria with or without branches. If branches were present the length and number of branches per mitochondrion were quantified. To quantify fission and fusion events cells were imaged every 10s for 2min. The time-lapse images were then examined frame by frame for any mitochondrial fission or fusion events. MEFs from at least 3 different individual embryos per genotype were examined.

Transmission Electron Microscopy and Quantification

Mice at 6, 12, or 22–25 months were anesthetized using avertin. Once anesthetized the mice underwent intra-peritoneal perfusion with PBS, followed by perfusion fixation with 4% PFA and 1.5% glutaraldehyde in 0.1 M Na-cacodylate buffer. The lower limb was removed and further fixed in the same solution at 4°C for 2 hours. *Tibialis Anterior* (TA) muscles were dissected and incubated overnight at 4°C in a secondary fix of 2.5% Glutaraldehyde in 0.1M Na-Cacodylate. Muscles were washed in Na-cacodylate buffer, post-fixed in 1% OsO_4 in 0.1 M Na-cacodylate for 1 hour, and rinsed in Na-cacodylate buffer. After dehydration with increasing concentrations of ethanol, muscles were embedded in Epon 812 resin. 65 nm ultrathin sections were stained with uranyl acetate and lead citrate and visualized on the transmission electron microscope (FEI Technai Spirt BioTWIN, Hillsboro, OR, USA) at 120kV. The samples were de-identified and Images were acquired in every field which contained non-overlapping muscle sections free from staining debris and free from section rips, fields were not repeat imaged to prevent overlap of quantification. All chemicals were purchased from Electron Microscopy Sciences, Hatfield, PA, USA. Quantification of mitochondria length:width ratio was done using Fiji's measurement tool [83], briefly mitochondria were measured on the longest axis for length and the widest axis for width. Z-disk alignment was measured using Fiji as performed by Gokhin et al. [83,20] briefly, the sarcomere length was measured from Z-disk to Z-disk the offset of Z-disks from neighboring sarcomeres was measured allowing for the determination of shift in Z-disks.

Mitochondrial Respiration

In these studies, muscle fiber bundles were used to assess mitochondrial respiration as this approach allows for the assessment of mitochondria in their native state[85]. The technique for preparing and permeabilizing muscle fiber bundles has previously been described [86].

12 month old mice were anesthetized and red portions of the gastrocnemius muscle were dissected and immediately added to ice-cold buffer × ([mM] − 7.23 K_2EGTA, 2.77 CaK_2EGTA, 20 imidazole, 20 taurine, 5.7 ATP, 14.3 phosphocreatine, 6.56 $MgCl_2{\cdot}6H_2O$, 50 MES, pH 7.1, 295 mosmol/kgH_2O). Under a dissecting microscope, connective tissue and fat were removed from the red portions before separating muscle into fiber bundles of ~ 1 mg wet wt. Muscle fiber bundles were then permeabilized in buffer × containing 30 μg/ml saponin for 30 min with continuous rotation at 4°C. Muscle fiber bundles were transferred to ice-cold buffer Z ([mM] – 110 K-MES, 35 KCl, 1 EGTA, $5K_2HPO_4$, 3 $MgCl_2{\cdot}6H_2O$, 5mg/ml BSA, pH 7.4, 295 mosmol/kgH_2O) and washed for 15 min at 4°C with continuous rotation.

Measurements of high-resolution O2 consumption were made using the OROBOROS Oxygraph-2K (Oroboros Instruments, Innsbruck, Austria) at 37°C with a starting oxygen concentration of ~350μM oxygen as previously described (Ryan et al. 2014). Experiments were conducted in buffer Z supplemented with 20mM creatine monohydrate and 25μM blebbistatin. Mitochondrial respiration was assessed by delivery of the substrates in the following order and at a final concentration of pyruvate 4mM, malate 2.5 mM, glutamate 5 mM, ADP 2.5 mM, succinate 5 mM, cytochrome c 5 μM, rotenone 10 μM, antimycin A 5 μM, ascorbic acid 2 mM and TMPD 0.5 mM (N,N,N',N'-Tetramethyl-p-phenylenediamine dihydrochloride). Preservation of mitochondrial membrane integrity was confirmed by excluding muscle bundles that produced a >10% increase in respiration in response to exogenous cytochrome c addition. Following completion of the protocol, muscle bundles were washed in distilled H2O, freeze-dried (Labconco, Kansas City, MO, USA) and weighed (Orion Cahn C-35, Thermo Electron, Beverly, MA). All chemicals and reagents were purchased from Sigma-Aldrich (St. Louis, MO, USA).

Maximum Succinate H_2O_2 production

In these studies, muscle fiber bundles were used to assess succinate induced H_2O_2 production. The technique for preparing and permeabilizing muscle fiber bundles is as described above [86]. 0.2–0.3mg dry weight of mouse muscle was combined with 30ug/ml saponin and incubated 30 minutes at 4°C. Amplex Red Assay Buffer [25μM], horseradish peroxidase [1U/ml] was added to the fibers and background was determined. Then succinate [10μM] and for the buffered solution inhibitors auranofin (AF) [1μM] and carmustine (BCNU) [100μM] were added. The Amplex Ultra Red Assay was run at 37°C with excitation/Emission of 565/600 for 10 seconds, with an integration time of 1 second.

Indirect calorimetry and body composition

22–25 month old male mice were individually housed for metabolic testing and were habituated to the metabolic chamber for 1 day prior to the collection of data over 2.5 days (n = 4–7). Oxygen consumption (VO2) and carbon dioxide production (VCO2), activity, and energy expenditure were measured using metabolic monitoring systems including the Oxymax Comprehensive Lab Animal Monitoring System (Columbus Instruments, Columbus, OH, USA). VO2 (volume O2), VCO2 (volume CO2), and respiratory exchange ratio (RER) were calculated from the gas-exchange data. Activity was measured on the x- and z-axes with the use of infrared beams. Mice were analyzed for total body fat, lean tissue,

and body water content using an EchoMRI quantitative magnetic resonance system (Echo Medical Systems, Houston, TX, USA). Energy expenditure was calculated with the formula provided by the manufacturer, expressed as Kcal/h and analyzed with body weight as continuous predictors in an ANCOVA model [87].

MAM Fractionation

Mouse liver from 12 month male animals was fractionated according to the protocol in Wieckowski et al [35]. Briefly: the mouse was anesthetized using avertin, sacrificed by cervical dislocation. The liver was immediately removed and successively washed in buffer (225mM mannitol, 75-mM sucrose, 0.5% BSA, 0.5mM EGTA and 30mM Tris-HCL, followed by 225mM mannitol, 75-mM sucrose, 0.5% BSA, and 30mM Tris-HCL, and 225mM mannitol, 75-mM sucrose, and 30mM Tris-HCL). The liver was minced, homogenized using a Teflon and glass mortar and pestle at 4°C, and spun at 740g for 5min, supernatant was collected and respun under the same conditions. The supernatant was collected and spun at 9,000×g for 10min, the pellet contains the crude mitochondria (the supernatant containing the cytoplasm and ER were centrifuged at 20,000×g for 30min, the supernatant was spun for 1h at 100,000×g, the resulting supernatant is the cytoplasmic fraction and the pellet is the ER fraction). The pellet containing the crude mitochondria was washed and spun at 10,000×g for 10min twice. The washed pellet was gently homogenized in buffer and layered on top of percoll media. The fractionation of the crude mitochondria into pure mitochondria and MAM was done by centrifuging the percoll layered suspension at 95,000×g for 30min using a swinging rotor (SW32 Beckman-Coulter, Brea, CA, USA). The resulting upper band (the MAM) and lower band (pure mitochondria) were each collected, washed, and centrifuged at 6,300×g for 10 min. The pellet from the pure mitochondrial sample was collected. The MAM supernatant was centrifuged at 100,000×g for 1h, the pellet was the MAM fraction (rotor 50.2 Beckman-Coulter, Brea, CA, USA). All spins were done at 4°C in a Beckman JS-HS high-speed centrifuge (20,000×g and under) or Beckman L8-M ultra high-speed centrifuge (over 20,000×g). All reagents from Sigma-Aldrich, St. Louis, MO, USA.

Western Blotting

12 or 22–25 month old male mice were anesthetized using avertin and sacrificed by cervical dislocation. The whole *quadriceps femoris* muscle was immediately dissected and any fat or connective tissue was removed. Protein was then extracted through mechanical tissue disruption via homogenization in liquid nitrogen and chemical disruption using 1%SDS buffer in 1×PBS with a cocktail of protease inhibitors (Aprotinin 100uM, Benzamide 0.79mg/mL, E-64 10nM, Leupeptin 10uM, Pepstatin 0.1mg/mL, PMSF 1mM; Sigma-Aldrich, St. Louis, MO, USA). Lysate was boiled for 5 min and centrifuged at 20,000×g for 3 min to remove the insoluble fraction. Protein concentration was determined by A280 on a NanoDrop ND-1000 Spectrometer (Thermo Fisher Scientific; Waltham, MA, USA). For comparison of relative immunoreactivities, 40ug of protein lysate was run on a 10% polyacrylamide gel for 1h at 150v. Samples were transferred onto PVDF membrane for 1h at 100v. Antibodies to ATP5A (ab14748; Abcam, Milton, Cambridge, UK), BiP (C50B12; Cell Signaling Technology, Danvers, MA, USA), β_{cyto}-Actin AC-15 (A5441; Sigma-Aldrich, St. Louis, MO, USA), γ_{cyto}-Actin (mAb 2–4; as published in [37]), Cytochrome C (ab13575;

Abcam, Milton, Cambridge, UK), calsequestrin (3516; Abcam, Milton, Cambridge, UK), Fis1 (HPA017430; Sigma-Aldrich, St. Louis, MO, USA), OPA1 (612606; BD Biosciences, San Jose, CA, USA), MFN2 (D2D10; Cell Signaling Technology, Danvers, MA, USA), FACL4 (ab155282; Abcam, Milton, Cambridge, UK), desmin (D1033; Sigma-Aldrich, St. Louis, MO, USA), GAPDH (Sigma-Aldrich, St. Louis, MO, USA), IP3R-3 (610312; BD Biosciences), IRE1α (14C10; Cell Signaling Technology, Danvers, MA, USA), PDI (C81H6; Cell Signaling Technology, Danvers, MA, USA), PERK (D11A8; Cell Signaling Technology, Danvers, MA, USA), SDHA (ab14715; Abcam, Milton, Cambridge, UK), SERCA1 (ab2819; Abcam, Milton, Cambridge, UK), sAmk1 (ARP42566-T100; Aviva Systems Biology, San Diego, CA, USA), Tubulin B512 (T6074; Sigma-Aldrich, St. Louis, MO, USA), and UQCR (ab110252; Abcam, Milton, Cambridge, UK), were used at the recommendation concentrations. Membranes were imaged on a Licor Odyssey (Lincoln, NE, USA).

In Vitro Contraction

Mice were anesthetized with sodium pentobarbital (100 mg/kg BW; Diamondback Drugs, Socttsdale, AZ, USA). *Extensor Digitorium Longus* (EDL) muscles were removed from 12 and 22–25 month old mice and mounted on a dual-mode muscle lever system (300B-LR; Aurora Scientific Inc., Aurora, ON, Canada) with 5-0 suture in a 1.5 mL bath assembly and filled with oxygenated (95 % O_2) Krebs Ringer bicarbonate buffer that was maintained at 25 °C. Muscles were adjusted to their anatomic optimal length (L_o) based on resting tension. Muscle length was then measured from myotendinous junction to myotendinous junction using digital calipers. Muscles remained quiescent in the bath for 5 min before beginning a protocol for testing contractile function. Maximal isometric tetanic contractions (P_o) were performed every 2 min until plateaued by stimulating the muscle for 200ms at 150Hz (Grass S48 stimulator delivered through a SIU5D stimulus isolation unit; Grass Telefactor, Warwick, RI, USA). Peak twitch force was measured by stimulating the muscle with a 0.5-ms pulse at 150 V. A second twitch was elicited 30s later followed 30s later by an isometric tetanic contraction. Every two minutes, isometric tetanic contractions were performed until the muscle reached a plateau of force (three contractions within 0.98 mN). Maximal rates of contraction and relaxation were derived from the slopes of the force-time traces. Two minutes of rest were followed by a fatigue protocol of submaximal (60Hz) isometric contractions every 7.5s for 200ms over 5min. Fatigue recovery was monitored by isometric tetanic contractions (200ms at 150 Hz) every 5min for 30min.

SERCA Activity

SR fractions were purified from muscle using the procedure outlined above. An enzyme-coupled, NADH-linked ATPase assay was used to measure SERCA ATPase activity in 96-well micro-plates. Each well contained 50 mM MOPS (pH 7.0), 100 mM KCl, 1 mM EGTA, 0.2 mM NADH, 1 mM phosphoenol pyruvate, 10 IU/mL pyruvate kinase, 10 IU/mL lactate dehydrogenase, 7uM calcium ionophore A23187, and CaCl2 added to set free [Ca2+] to the desired values. Then, 1.0 μg mouse skeletal SR vesicles was used in each well. The assay was started upon the addition of magnesium adenosine triphosphate (MgATP) at a final concentration of 5 mM and read in a SpectraMax Plus microplate spectrophotometer (Molecular Devices, Sunnyvale, CA, USA), bringing the total volume to 200 μL.

Inhibition of SERCA activity was evaluated in mouse skeletal SR vesicles. Thapsigargan was dissolved in DMSO and adjusted to 100 times the concentration used in the final assay wells. Then, either 2uL of compound or DMSO only was added to each well to keep the final [DMSO] at 1% (v/v) during the assay. A 20min incubation at room temperature with the compound/DMSO, assay mix mentioned above, and skeletal SR vesicles was conducted prior to adding MgATP and read in a SpectraMax Plus microplate spectrophotometer (Molecular Devices, Sunnyvale, CA, USA).

Acknowledgments

The Characterization Facility at the University of Minnesota for TEM sample preparation.

Maria Razzoli and Alessandro Bartolomucci at the Integrated Biology and Physiology Core at the University of Minnesota for whole body respirometry. Ji Li for experimental design and analysis of SERCA activity data.

Our funding sources: a NIH grant AR049899 to J.M. Ervasti, a NIH grant AR066660 to E. E. Spangenburg, a Pilot and Feasibility grant to B.J. Perrin awarded through NIH P30 AR057220, and a NIH training grant AG029796 to D.M. Nelson.

Abbreviations

SR	Sarcoplasmic Reticulum
ER	Endoplasmic reticulum
MEF	Mouse Embryonic Fibroblast
TEM	transmission electron microscopy
EDL	extensor digitorum longus
MAMs	Mitochondrial associated membranes
SERCA	sarco-/endo - plasmic reticulum Ca2+ - ATPase
ms	muscle specific
KO	knockout
RCR	respiratory control ratio
CT	control
UPR	unfolded protein response
ROS	reactive oxygen species
RYR	ryanodine receptor
UTR	untranslated region
RER	respiratory exchange ratio
PDI	protein disulfide isomerase

IRE1α	inositol-requiring enzyme 1
BiP	binding immunoglobulin protein
PERK	protein kinase RNA-like endoplasmic reticulum kinase
FACL4	long-chain-fatty-acid-CoA ligase 4
UQCR	ubiquinol Cytochrome c Reductase
IP3R-3	inositol 1, 4, 5-trisphosphate
ATP5A	ATP synthase subunit alpha

Bibliography

1. Kumar A, Crawford K, Close L, Madison M, Lorenz J, Doetschman T, Pawlowski S, Duffy J, Neumann J, Robbins J, Boivin GP, O'Toole BA, Lessard JL. Rescue of cardiac a-actin-deficient mice by enteric smooth muscle g-actin. Proc. Natl. Acad. Sci. U. S. A. 1997; 94:4406–4411. [PubMed: 9114002]
2. Crawford K, Flick R, Close L, Shelly D, Paul R, Bove K, Kumar A, Lessard J. Mice lacking skeletal muscle actin show reduced muscle strength and growth deficits and die during the neonatal period. Mol. Cell Biol. 2002; 22:5887–5896. [PubMed: 12138199]
3. Schwartz R, Rothblum K. Gene switching in myogenesis: differential expression of the chicken actin multigene family. Biochemistry. 1981; 20:4122–4129. [PubMed: 7284314]
4. McHugh K, Crawford K, Lessard J. A comprehensive analysis of the developmental and tissue-specific expression of the isoactin multigene family in the rat. Dev. Biol. 1991; 148:442–458. [PubMed: 1743394]
5. Lloyd C, Schevzov G, Gunning P. Transfection of nonmuscle beta- and gamma-actin genes into myoblasts elicits different feedback regulatory responses from endogenous actin genes. J. Cell Biol. 1992; 117:775–785. [PubMed: 1577857]
6. Peckham M. Engineering a multi-nucleated myotube, the role of the actin cytoskeleton. J. Microsc. 2008; 231:486–493. [PubMed: 18755004]
7. Nowak SJ, Nahirney PC, Hadjantonakis A-K, Baylies MK. Nap1-mediated actin remodeling is essential for mammalian myoblast fusion. J. Cell Sci. 2009; 122:3282–3293. [PubMed: 19706686]
8. Duan R, Gallagher PJ. Dependence of myoblast fusion on a cortical actin wall and nonmuscle myosin IIA. Dev. Biol. 2009; 325:374–85. [PubMed: 19027000]
9. Craig SW, Pardo JV. Gamma actin, spectrin, and intermediate filament proteins colocalize with vinculin at costameres, myofibril-to-sarcolemma attachment sites. Cell Motil. 1983; 3:449–462. [PubMed: 6420066]
10. Otey CA, Kalnoski M, Bulinski JC. Immunolocalization of muscle and nonmuscle isoforms of actin in myogenic cells and adult skeletal muscle. Cell Motil. Cytoskeleton. 1988; 9:337–348. [PubMed: 3292062]
11. Rybakova IN, Patel JR, Ervasti JM. The dystrophin complex forms a mechanically strong link between the sarcolemma and costameric actin. J. Cell Biol. 2000; 150:1209–14. [PubMed: 10974007]
12. Prins KW, Call Ja, Lowe Da, Ervasti JM. Quadriceps myopathy caused by skeletal muscle-specific ablation of β(cyto)-actin. J. Cell Sci. 2011; 124:951–7. [PubMed: 21325027]
13. Kee AJ, Schevzov G, Nair-Shalliker V, Robinson CS, Vrhovski B, Ghoddusi M, Qiu MR, Lin JJ-C, Weinberger R, Gunning PW, Hardeman EC. Sorting of a nonmuscle tropomyosin to a novel cytoskeletal compartment in skeletal muscle results in muscular dystrophy. J. Cell Biol. 2004; 166:685–96. [PubMed: 15337777]

14. Gokhin DS, Lewis Ra, McKeown CR, Nowak RB, Kim NE, Littlefield RS, Lieber RL, Fowler VM. Tropomodulin isoforms regulate thin filament pointed-end capping and skeletal muscle physiology. J. Cell Biol. 2010; 189:95–109. [PubMed: 20368620]
15. Papponen H, Kaisto T, Leinonen S, Kaakinen M, Metsikkö K. Evidence for gamma-actin as a Z disc component in skeletal myofibers. Exp. Cell Res. 2009; 315:218–25. [PubMed: 19013151]
16. Nakata T, Nishina Y, Yorifuji H. Cytoplasmic gamma actin as a Z-disc protein. Biochem. Biophys. Res. Commun. 2001; 286:156–63. [PubMed: 11485322]
17. Ayalon G, Davis JQ, Scotland PB, Bennett V. An ankyrin-based mechanism for functional organization of dystrophin and dystroglycan. Cell. 2008; 135:1189–200. [PubMed: 19109891]
18. Almenar-Queralt A, Lee A. Identification of a novel tropomodulin isoform, skeletal tropomodulin, that caps actin filament pointed ends in fast skeletal muscle. J. Biol. Chem. 1999; 274:28466–28475. [PubMed: 10497209]
19. Vlahovich N, Kee AJ, Van der Poel C, Kettle E, Hernandez-Deviez D, Lucas C, Lynch GS, Parton RG, Gunning PW, Hardeman EC. Cytoskeletal tropomyosin Tm5NM1 is required for normal excitation-contraction coupling in skeletal muscle. Mol. Biol. Cell. 2009; 20:400–9. [PubMed: 19005216]
20. Gokhin DS, Fowler VM. Cytoplasmic gamma-actin and tropomodulin isoforms link to the sarcoplasmic reticulum in skeletal muscle fibers. J. Cell Biol. 2011; 194:105–20. [PubMed: 21727195]
21. Vassilopoulos S, Gentil C, Lainé J, Buclez P-O, Franck A, Ferry A, Précigout G, Roth R, Heuser JE, Brodsky FM, Garcia L, Bonne G, Voit T, Piétri-Rouxel F, Bitoun M. Actin scaffolding by clathrin heavy chain is required for skeletal muscle sarcomere organization. J. Cell Biol. 2014; 205:377–93. [PubMed: 24798732]
22. Wang L, Miao J, Li L, Wu D, Zhang Y, Peng Z, Zhang L, Yuan Z, Sun K. Identification of an FHL1 protein complex containing gamma-actin and non-muscle myosin IIB by analysis of protein-protein interactions. PLoS One. 2013; 8:e79551. [PubMed: 24265776]
23. Domenighetti AA, Chu PH, Wu T, Sheikh F, Gokhin DS, Guo LT, Cui Z, Peter AK, Christodoulou DC, Parfenov MG, Gorham JM, Li DY, Banerjee I, Lai X, Witzmann FA, Seidman CE, Seidman JG, Gomes A V, Shelton GD, Lieber RL, Chen J. Loss of FHL1 induces an age-dependent skeletal muscle myopathy associated with myofibrillar and intermyofibrillar disorganization in mice. Hum. Mol. Genet. 2014; 23:209–225. [PubMed: 23975679]
24. Sonnemann KJ, Fitzsimons DP, Patel JR, Liu Y, Schneider MF, Moss RL, Ervasti JM. Cytoplasmic gamma-actin is not required for skeletal muscle development but its absence leads to a progressive myopathy. Dev. Cell. 2006; 11:387–97. [PubMed: 16950128]
25. Korobova F, Ramabhadran V, Higgs HN. An actin-dependent step in mitochondrial fission mediated by the ER-associated formin INF2. Science. 2013; 339:464–7. [PubMed: 23349293]
26. Manor U, Bartholomew S, Golani G, Christenson E, Kozlov M, Higgs H, Spudich J, Lippincott-schwartz J. A mitochondria-anchored isoform of the actin-nucleating spire protein regulates mitochondrial division. Elife. 2015; 4:1–27.
27. Vlahovich N, Kee AJ, Poel C Van Der, Kettle E, Hernandez-deviez D, Lucas C, Lynch GS, Parton RG, Gunning PW, Hardeman EC. Cytoskeletal Tropomyosin Tm5NM1 Is Required for Normal Excitation – Contraction Coupling in Skeletal Muscle. 2009; 20:400–409.
28. Milner DJ, Mavroidis M, Weisleder N, Capetanaki Y. Desmin cytoskeleton linked to muscle mitochondrial distribution and respiratory function. J. Cell Biol. 2000; 150:1283–1297. [PubMed: 10995435]
29. Winter L, Wittig I, Peeva V, Eggers B, Heidler J, Chevessier F, Kley RA, Barkovits K, Strecker V, Berwanger C, Herrmann H, Marcus K, Kornblum C. Mutant desmin substantially perturbs mitochondrial morphology, function and maintenance in skeletal muscle tissue. Acta Neuropathol. 2016; 132:453–473. [PubMed: 27393313]
30. Rizzuto R, Pinton P, Carrington W, Fay FS, Fogarty KE, Lifshitz LM, Tuft RA, Pozzan T. Close Contacts with the Endoplasmic Reticulum as Determinants of Mitochondrial Ca2+ Responses. Science (80-.). 1998; 280:1763–1766.

31. Wieckowski MR, Pinton P, Rizzuto R, Duszyn J. Overexpression of adenine nucleotide translocase reduces Ca 2+ signal transmission between the ER and mitochondria. Biochem. Biophys. Res. Commun. 2006; 348:393–399. [PubMed: 16887100]
32. Brito OM, De, Scorrano, L. Mitofusin 2 tethers endoplasmic reticulum to mitochondria. Nature. 2008; 456:605–610. [PubMed: 19052620]
33. Raturi A, Simmen T. Biochimica et Biophysica Acta Where the endoplasmic reticulum and the mitochondrion tie the knot : The mitochondria-associated membrane (MAM) ☆. BBA - Mol. Cell Res. 2013; 1833:213–224.
34. Patergnani S, Suski JM, Agnoletto C, Bononi A, Bonora M, De Marchi E, Giorgi C, Marchi S, Missiroli S, Poletti F, Rimessi A, Duszynski J, Wieckowski MR, Pinton P. Calcium signaling around Mitochondria Associated Membranes (MAMs). Cell Commun. Signal. 2011; 9:19–29. [PubMed: 21939514]
35. Wieckowski MR, Giorgi C, Lebiedzinska M, Duszynski J, Pinton P. Isolation of mitochondria-associated membranes and mitochondria from animal tissues and cells. Nat. Protoc. 2009; 4:1582–90. [PubMed: 19816421]
36. Patrinostro X, O'Rourke AR, Chamberlain CM, Moriarity BS, Perrin BJ, Ervasti JM. Relative importance of βcyto- and γ cyto-actin in primary mouse embryonic fibroblasts. Mol. Biol. Cell. 2017
37. Hanft LM, Bogan DJ, Mayer U, Kaufman SJ, Kornegay JN, Ervasti JM. Cytoplasmic gamma-actin expression in diverse animal models of muscular dystrophy. Neuromuscul. Disord. 2007; 17:569–74. [PubMed: 17475492]
38. Lewin TM, Kim J, Granger DA, Vance JE, Coleman RA. Acyl-CoA Synthetase Isoforms 1, 4, and 5 Are Present in Different Subcellular Membranes in Rat Liver and Can Be Inhibited Independently *. J. Biol. Chem. 2001; 276:24674–24679. [PubMed: 11319232]
39. Krisans SK, Coleman RA. Rat liver acyl-CoA synthetase 4 is a peripheral-membrane protein located in two distinct subcellular organelles, peroxisomes, and mitochondrial-associated membrane. Arch. Biochem. Biophys. 2002; 404:263–270. [PubMed: 12147264]
40. Westermann B. Mitochondrial fusion and fission in cell life and death. Nat. Publ. Gr. 2010; 11:872–884.
41. De Vos KJ, Allan VJ, Grierson AJ, Sheetz MP. Mitochondrial function and actin regulate dynamin-related protein 1-dependent mitochondrial fission. Curr. Biol. 2005; 15:678–83. [PubMed: 15823542]
42. Pfluger PT, Kabra DG, Aichler M, Schriever SC, Pfuhlmann K, García VC, Lehti M, Weber J, Kutschke M, Rozman J, Elrod JW, Hevener AL, Feuchtinger A, Hrabě De Angelis M, Walch A, Rollmann SM, Aronow BJ, Müller TD, Perez-Tilve D, Jastroch M, De Luca M, Molkentin JD, Tschöp MH. Calcineurin Links Mitochondrial Elongation with Energy Metabolism. Cell Metab. 2015; 22:838–850. [PubMed: 26411342]
43. Valente AJ, Maddalena LA, Robb EL, Moradi F, Stuart JA. A simple ImageJ macro tool for analyzing mitochondrial network morphology in mammalian cell culture. Acta Histochem. 2017; 119:315–326. [PubMed: 28314612]
44. Anesti V, Scorrano L. The relationship between mitochondrial shape and function and the cytoskeleton. Biochim. Biophys. Acta - Bioenerg. 2006; 1757:692–699.
45. Chen H, Chan DC. Emerging functions of mammalian mitochondrial fusion and fission. 2005; 14:283–289.
46. Chen H, Detmer SA, Ewald AJ, Griffin EE, Fraser SE, Chan DC. Mitofusins Mfn1 and Mfn2 coordinately regulate mitochondrial fusion and are essential for embryonic embryonic development. J. Cell Biol. 2000; 160:189–200.
47. Brown M, Hasser EM. Complexity of age-related change in skeletal muscle. J. Gerontol. A. Biol. Sci. Med. Sci. 1996; 51:B117–23. [PubMed: 8612095]
48. Ebashi S, Endo M. Calcium ion and muscle contraction. Prog. Biophys. Mol. Biol. 1968; 18:123–183. [PubMed: 4894870]
49. Stephenson DG, Lamb GD, Stephenson GMM. Events of the excitation-contraction-relaxation (E-C-R) cycle in fast- and slow-twitch mammalian muscle fibres relevant to muscle fatigue. Acta Physiol. Scand. 1998; 162:229–245. [PubMed: 9578368]

50. Odermatt A, Taschner P, Khanna V, Busch H, Karpati G, Jablecki C, Breuning M, MacLennan D. Mutations in the gene-encoding SERCA1, the fast-twitch skeletal muscle sarcoplasmic reticulum Ca2+ ATPase, are associated with Brody disease. Nat. Genet. 1996; 14:191–4. [PubMed: 8841193]
51. Desmond PF, Muriel J, Markwardt ML, Rizzo MA, Bloch RJ. Identification of small ankyrin 1 as a novel sarco(endo)plasmic reticulum Ca2+-ATPase 1 (SERCA1) regulatory protein in skeletal muscle. J. Biol. Chem. 2015; 290:27854–27867. [PubMed: 26405035]
52. Liang S-H, Zhang W, McGrath BC, Zhang P, Cavener DR. PERK (eIF2alpha kinase) is required to activate the stress-activated MAPKs and induce the expression of immediate-early genes upon disruption of ER calcium homoeostasis. Biochem. J. 2006; 393:201–9. [PubMed: 16124869]
53. Ma Y, Hendershot LM. The unfolding tale of the unfolded protein response. Cell. 2001; 107:827–830. [PubMed: 11779459]
54. Niwa M, Walter P. Pausing to decide. Proc. Natl. Acad. Sci. U. S. A. 2000; 97:12396–12397. [PubMed: 11058174]
55. Schröder M. Endoplasmic reticulum stress responses. Cell. Mol. Life Sci. 2008; 65:862–894. [PubMed: 18038217]
56. Hanft LM, Rybakova IN, Patel JR, Rafael-Fortney Ja, Ervasti JM. Cytoplasmic gamma-actin contributes to a compensatory remodeling response in dystrophin-deficient muscle. Proc. Natl. Acad. Sci. U. S. A. 2006; 103:5385–90. [PubMed: 16565216]
57. Eisner V, Lenaers G, Hajnóczky G. Mitochondrial fusion is frequent in skeletal muscle and supports excitation-contraction coupling. J. Cell Biol. 2014; 205:179–195. [PubMed: 24751540]
58. Mishra P, Chan DC. Metabolic regulation of mitochondrial dynamics. J. Cell Biol. 2016; 212:379–387. [PubMed: 26858267]
59. Chen H, Ren S, Clish C, Jain M, Mootha V, McCaffery JM, Chan DC. Titration of mitochondrial fusion rescues Mff-deficient cardiomyopathy. J. Cell Biol. 2015; 211:795–805. [PubMed: 26598616]
60. Eisner V, Csordas G, Hajnoczky G. Interactions between sarco-endoplasmic reticulum and mitochondria in cardiac and skeletal muscle - pivotal roles in Ca(2)(+) and reactive oxygen species signaling. J. Cell Sci. 2013; 126:2965–2978. [PubMed: 23843617]
61. Csordás G, Hajnóczky G. SR/ER-mitochondrial local communication: Calcium and ROS. Biochim. Biophys. Acta - Bioenerg. 2009; 1787:1352–1362.
62. Glancy B, Hartnell LM, Malide D, Yu Z-X, Combs CA, Connelly PS, Subramaniam S, Balaban RS. Mitochondrial reticulum for cellular energy distribution in muscle. Nature. 2015; 523:617–620. [PubMed: 26223627]
63. Spät A, Szanda G, Csordás G, Hajnóczky G. High- and low-calcium-dependent mechanisms of mitochondrial calcium signalling. Cell Calcium. 2008; 44:51–63. [PubMed: 18242694]
64. Chami M, Oulès B, Szabadkai G, Tacine R, Rizzuto R, Paterlini-Bréchot P. Role of SERCA1 Truncated Isoform in the Proapoptotic Calcium Transfer from ER to Mitochondria during ER Stress. Mol. Cell. 2008; 32:641–651. [PubMed: 19061639]
65. Ermak G, Davies KJ. Calcium and oxidative stress: from cell signaling to cell death. Mol Immunol. 2002; 38:713–721. [PubMed: 11841831]
66. Rizzuto R, Pinton P, Carrington W, Fay FS, Fogarty KE, Lifshitz LM, Tuft RA, Pozzan T, Lawrie AM, Rizzuto R, Pozzan T, Simpson AWM, Rutter GA, Drummond RM, Fay FS, Jouaville LS, Pozzan T, Heim R, Tsien RY, Rizzuto R, Carrington WA, Nunnari J, Montero M, MacDonald MJ, Brown LJ, Rizzuto R, Kass GEN. Close contacts with the endoplasmic reticulum as determinants of mitochondrial Ca2+ responses. Science (80-.). 1998; 280:1763–6.
67. Burté F, Carelli V, Chinnery PF, Yu-Wai-Man P. Disturbed mitochondrial dynamics and neurodegenerative disorders. Nat. Rev. Neurol. 2014; 11:11–24. [PubMed: 25486875]
68. Gilady SY, Bui M, Lynes EM, Benson MD, Watts R, Vance JE, Simmen T. Ero1α requires oxidizing and normoxic conditions to localize to the mitochondria-associated membrane (MAM). Cell Stress Chaperones. 2010; 15:619–629. [PubMed: 20186508]
69. Grimm S. The ER-mitochondria interface: The social network of cell death. Biochim. Biophys. Acta - Mol. Cell Res. 2012; 1823:327–334.

70. Kornmann B, Currie E, Collins SR, Schuldiner M, Nunnari J, Weissman JS, Walter P. An ER-Mitochondria Tethering Complex Revealed by a Synthetic Biology Screen. Science (80-.). 2009; 325:477–481.
71. Li G, Mongillo M, Chin KT, Harding H, Ron D, Marks AR, Tabas I. Role of ERO1-α-mediated stimulation of inositol 1,4,5-triphosphate receptor activity in endoplasmic reticulum stress-induced apoptosis. J. Cell Biol. 2009; 186:783–792. [PubMed: 19752026]
72. Rusiñol AE, Cui Z, Chen MH, Vance JE. A unique mitochondria-associated membrane fraction from rat liver has a high capacity for lipid synthesis and contains pre-Golgi secretory proteins including nascent lipoproteins. J. Biol. Chem. 1994; 269:27494–27502. [PubMed: 7961664]
73. Dayanithi G, Chen-Kuo-Chang M, Viero C, Hamel C, Muller A, Lenaers G. Characterization of Ca2+ signalling in postnatal mouse retinal ganglion cells: involvement of OPA1 in Ca2+ clearance. Ophthalmic Genet. 2010; 31:53–65. [PubMed: 20450306]
74. Singaravelu K, Nelson C, Bakowski D, De Brito OM, Ng SW, Di Capite J, Powell T, Scorrano L, Parekh AB. Mitofusin 2 regulates STIM1 migration from the Ca2+ store to the plasma membrane in cells with depolarized mitochondria. J. Biol. Chem. 2011; 286:12189–12201. [PubMed: 21220420]
75. Kushnareva YE, Gerencser AA, Bossy B, Ju W-K, White AD, Waggoner J, Ellisman MH, Perkins G, Bossy-Wetzel E. Loss of OPA1 disturbs cellular calcium homeostasis and sensitizes for excitotoxicity. Cell Death Differ. 2013; 20:353–65. [PubMed: 23138851]
76. Andersson DC, Betzenhauser MJ, Reiken S, Meli AC, Umanskaya A, Xie W, Shiomi T, Zalk R, Lacampagne A, Marks AR. Ryanodine receptor oxidation causes intracellular calcium leak and muscle weakness in aging. Cell Metab. 2011; 14:196–207. [PubMed: 21803290]
77. Lloyd C, Gunning P. Noncoding regions of the gamma-actin gene influence the impact of the gene on myoblast morphology. J. Cell Biol. 1993; 121:73–82. [PubMed: 8458874]
78. Rubenstein PA. The functional importance of multiple actin isoforms. BioEssays. 1990; 12:309–315. [PubMed: 2203335]
79. Zhang F, Saha S, Shabalina SA, Kashina A. Differential Arginylation of Actin Sequence – Dependent Degradation. Science (80-.). 2010; 1065:1534–1537.
80. Bergeron SE, Zhu M, Thiem SM, Friderici KH, Rubenstein PA. Ion-dependent polymerization differences between mammalian α- and β-nonmuscle actin isoforms. J. Biol. Chem. 2010; 285:16087–16095. [PubMed: 20308063]
81. Perrin BJ, Sonnemann KJ, Ervasti JM. β-Actin and γ-Actin are each dispensable for auditory hair cell development but required for stereocilia maintenance. PLoS Genet. 2010; 6:1–12.
82. Miniou P, Tiziano D, Frugier T, Roblot N, Meur M Le, Melki J. Gene targeting restricted to mouse striated muscle lineage. Nucleic Acids Res. 1999; 27:10–13. [PubMed: 9847131]
83. Schindelin J, Arganda-Carreras I, Frise E, Kaynig V, Longair M, Pietzsch T, Preibisch S, Rueden C, Saalfeld S, Schmid B, Tinevez J-Y, White DJ, Hartenstein V, Eliceiri K, Tomancak P, Cardona A. Fiji: an open-source platform for biological-image analysis. Nat. Methods. 2012; 9:676–682. [PubMed: 22743772]
84. Bunnell TM, Ervasti JM. Delayed embryonic development and impaired cell growth and survival in Actg1 null mice. Cytoskeleton. 2010; 67:564–72. [PubMed: 20662086]
85. Perry CGR, Kane DA, Lanza IR, Neufer PD. Methods for assessing mitochondrial function in diabetes. Diabetes. 2013; 62:1041–1053. [PubMed: 23520284]
86. Lark DS, Torres MJ, Lin C-T, Ryan TE, Anderson EJ, Neufer PD. Direct real-time quantification of mitochondrial oxidative phosphorylation efficiency in permeabilized skeletal muscle myofibers. Am. J. Physiol. - Cell Physiol. 2016; 311:C239–C245. [PubMed: 27335172]
87. Tschöp MH, Speakman JR, Arch JRS, Auwerx J, Brüning JC, Chan L, Eckel RH, Farese RV, Galgani JE, Hambly C, Herman Ma, Horvath TL, Kahn BB, Kozma SC, Maratos-Flier E, Müller TD, Münzberg H, Pfluger PT, Plum L, Reitman ML, Rahmouni K, Shulman GI, Thomas G, Kahn CR, Ravussin E. A guide to analysis of mouse energy metabolism. Nat. Methods. 2012; 9:57–63.

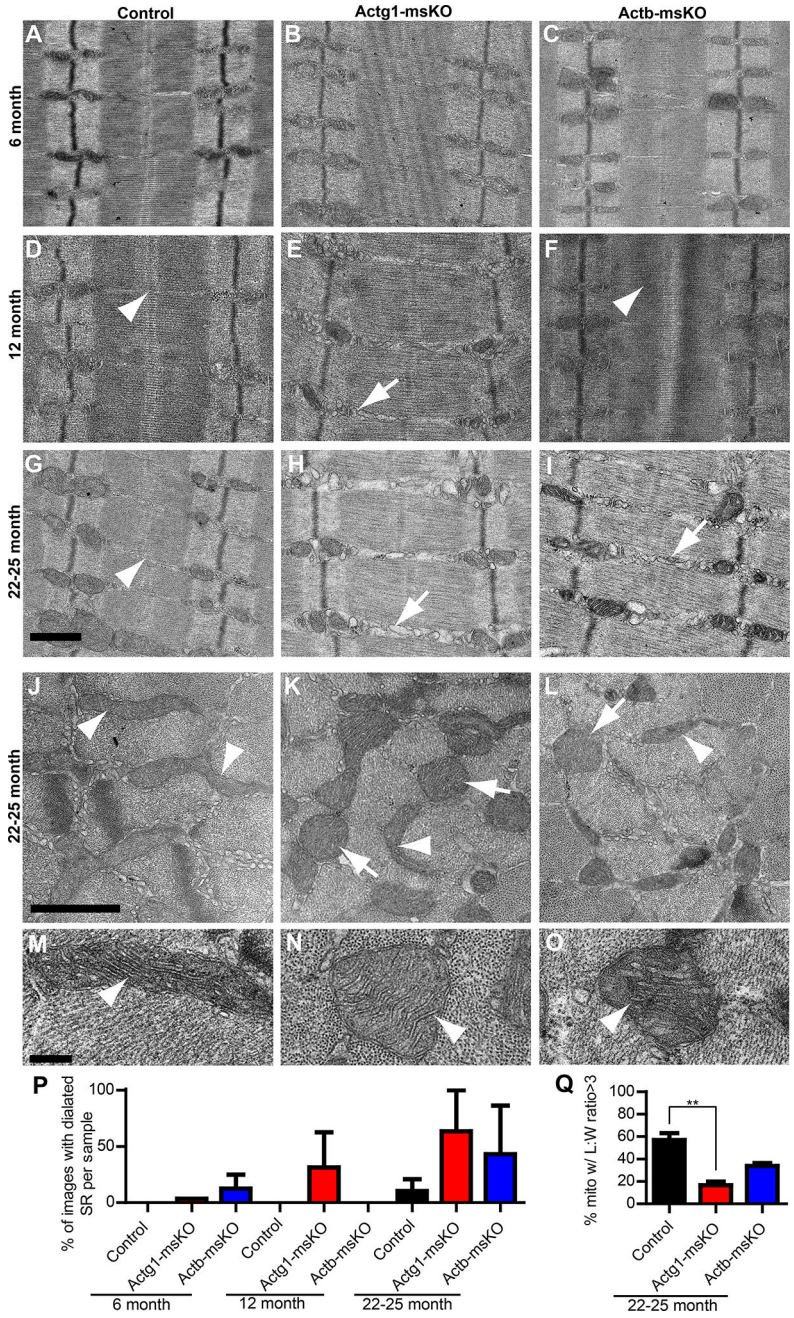

Figure 1. Altered sarcoplasmic reticulum and mitochondrial morphology in aged Actg1 and Actb KO skeletal muscle

(A–I) Longitudinal sections of TA from control, Actg1-msKO, and Actb-msKO mice at 6 (A–C), 12 (D–F), and 22–25 (G–I) months of age. White arrowheads denote normal SR, white arrows denote dilated SR. Scale bars = 1μm. (P) Quantification of the percentage of images examined that displayed dilated SR. (J–L) Transverse sections of TA from control, Actg1-msKO, and Actb-msKO mice at 22–25 months of age. Scale bars = 1μm. (M–O) High magnification image of mitochondria internal structure, white arrow heads denote cristae. Scale bar = 250nm. (Q) Quantification of mitochondrial length:width ratio. 1-way ANOVA

with Tukey's post hoc test were performed to determine significance. ** is $0.01<p<0.001$. Error bars are S.E.M.

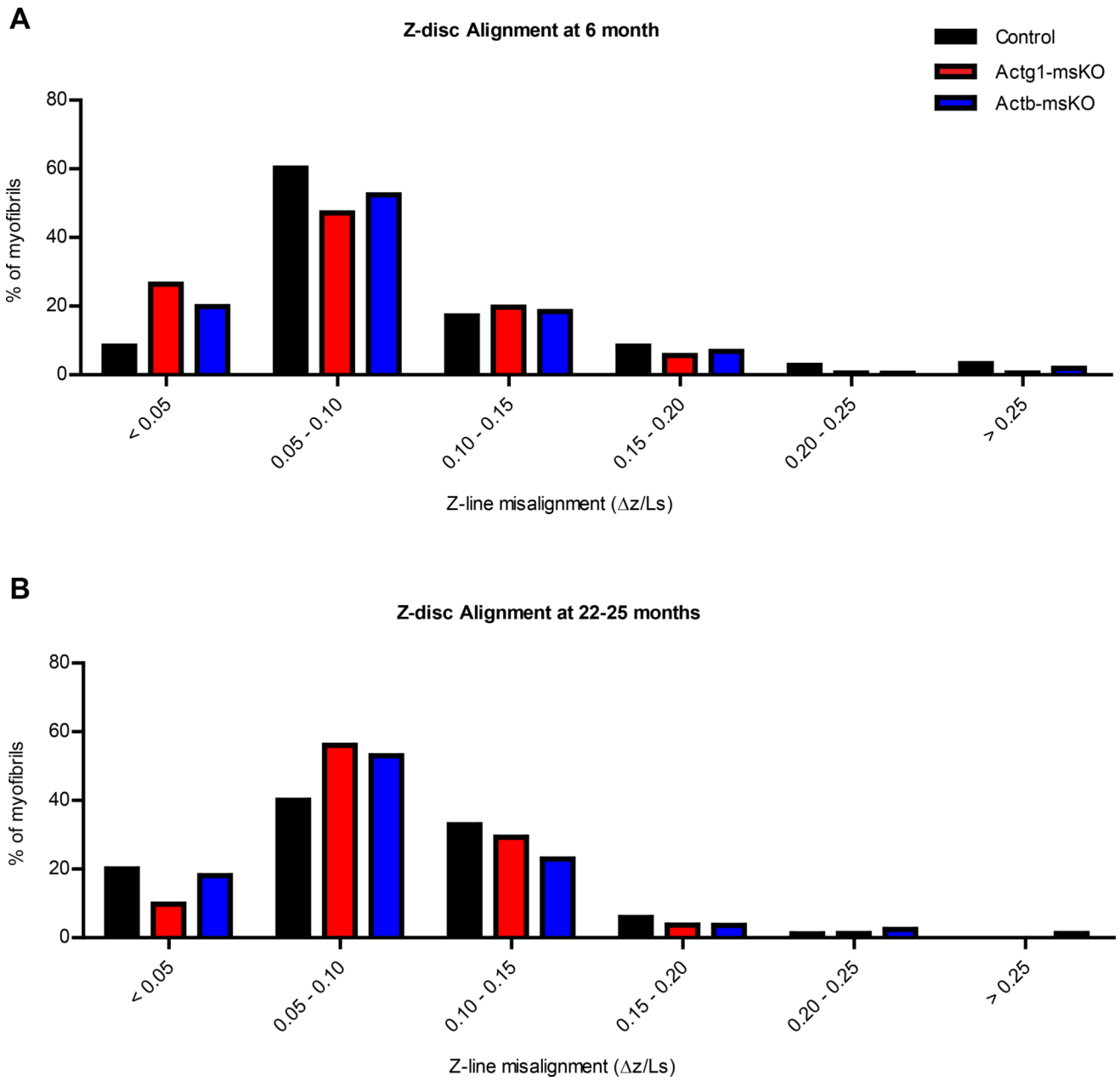

Figure 2. No shift in Z-disk Alignment in Actg1 and Actb KO skeletal muscle

Z-disk alignment of adjacent sarcomere pairs at 6 months (A) and 22–25 months (B). 2-way ANOVA determined no significant difference across genotypes.

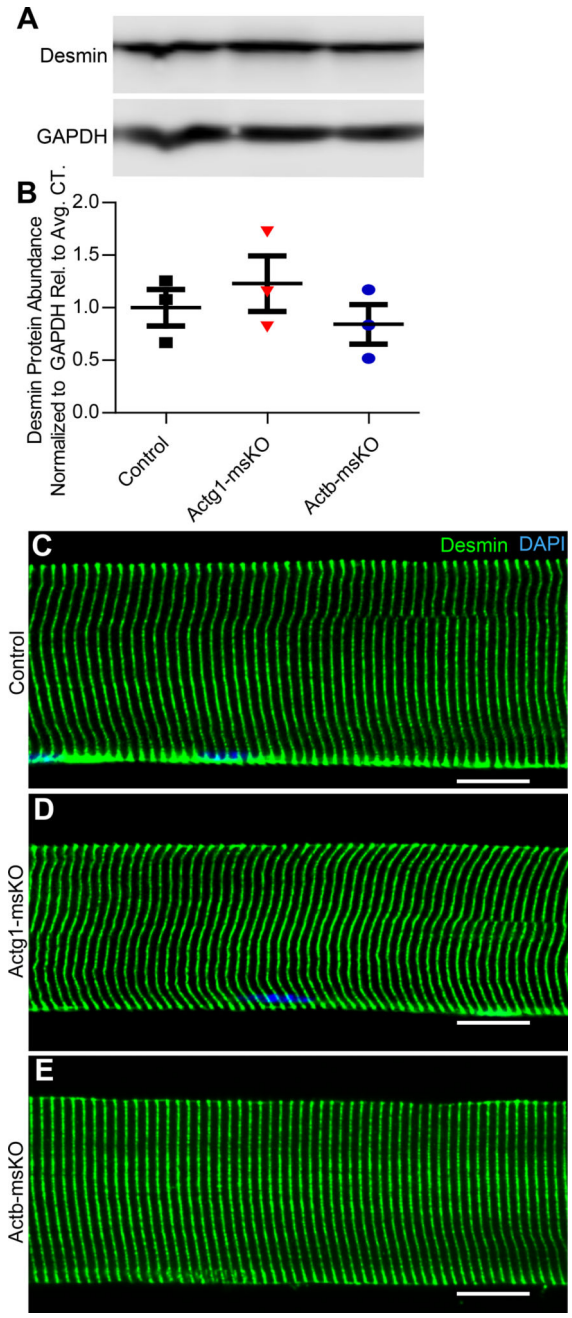

Figure 3. Unaltered desmin abundance and localization in Actg1 and Actb KO skeletal muscle

(A–B) Western blot against desmin in quadriceps muscle from control and Actg1-msKO and Actb-msKO animals and quantification of western blot, normalized to GAPDH and relative to the average of the control samples. 1-way ANOVA with Tukey's post hoc test determined no significant difference. (C–E) Representative isolated EDL muscle fibers stained for desmin localization in green and DAPI in blue. Scale bars = 20μm.

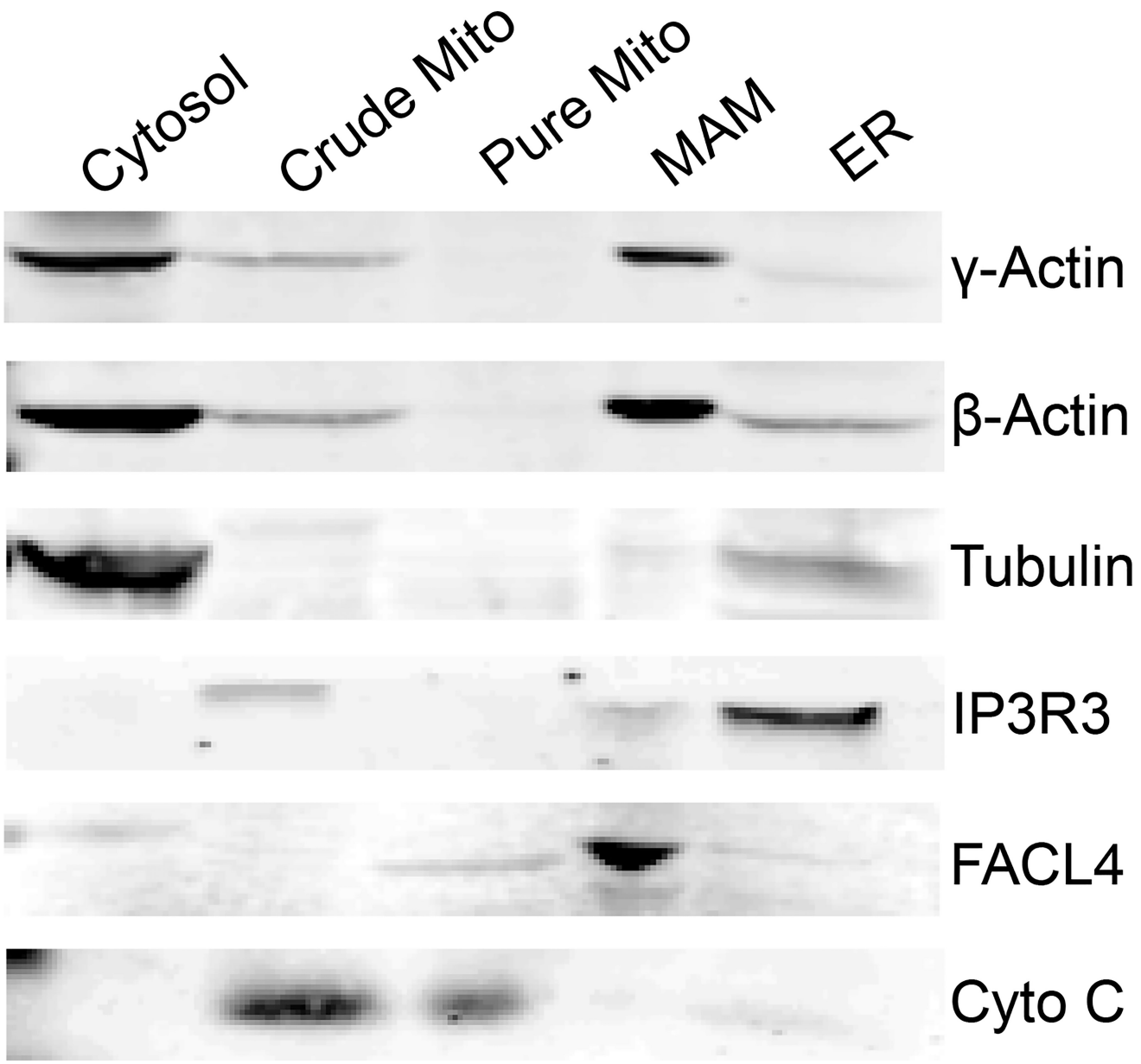

Figure 4. Enrichment of γ_{cyto}- and β_{cyto}-actin in isolated mitochondrial associated membrane

Shown are identical western blots loaded with equal amounts of protein from the fractions obtained during the preparation of isolated mitochondrial associated membranes from mouse liver and stained with antibodies to the indicated protein.

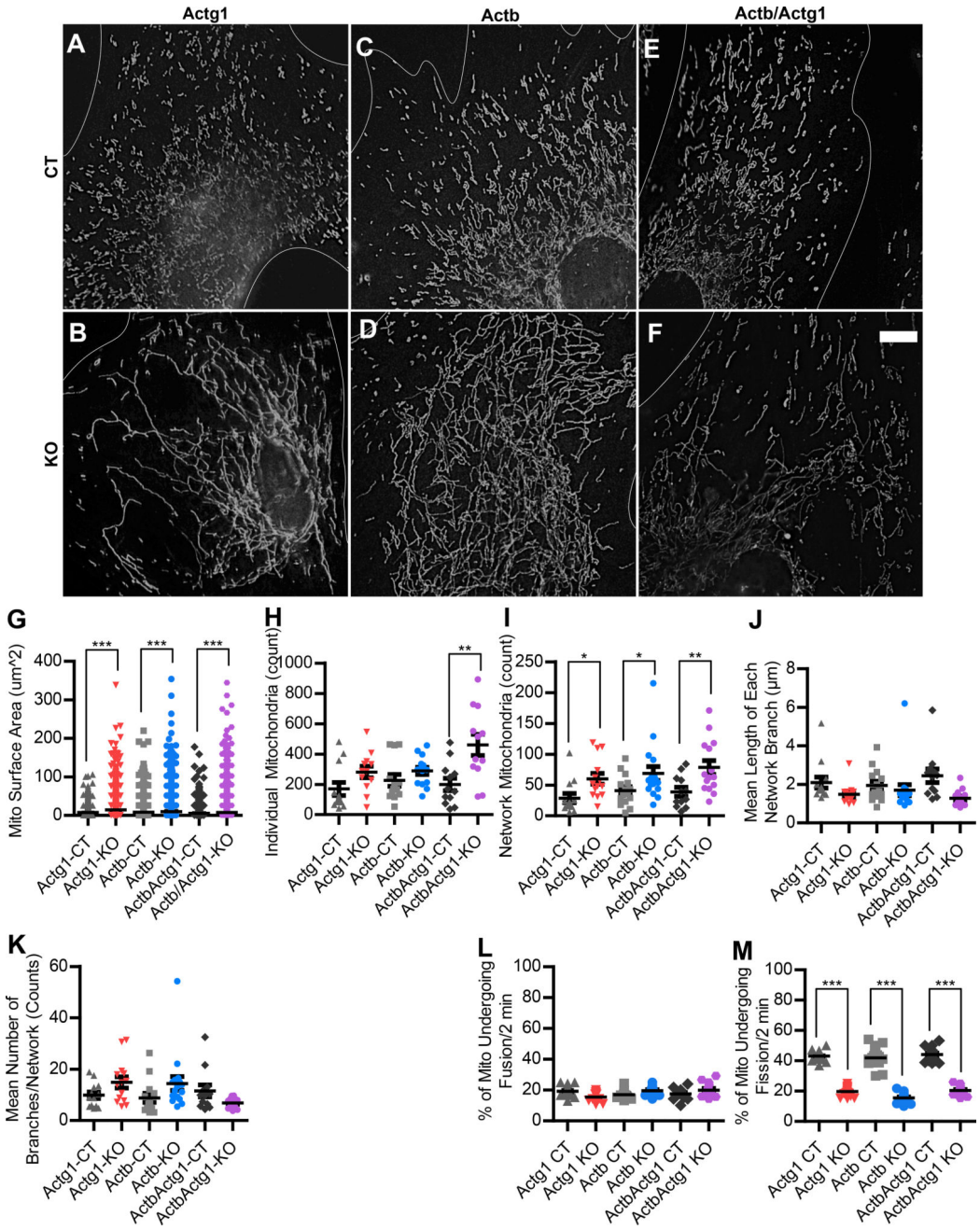

Figure 5. Ablation of γ_{cyto}- or β_{cyto}-actin results in increased mitochondrial area and decreased fission

(A–F) Mitochondria appear elongated in Actg1 KO Actb KO, and Actb/Actg1 dKO MEFs compared to control (CT). Scale bar = 10μm. (G) Surface area of each individual mitochondrion per genotype. (H) The number of individual (non-branched) mitochondria per genotype. (I) The number of network (branched) mitochondria per genotype. (J) The mean length of each branch off of a network mitochondria. (K) The mean number of branches on a network mitochondria. (L–M). Quantitation of fission and fusion frequencies in CT, Actg1 KO, Actb KO, and Actb/Actg1 dKO MEFs. 1-way ANOVA with Tukey's post hoc test determined significance * is $0.01<p<0.05$ and *** is $p<0.001$. Error bars are S.E.M.

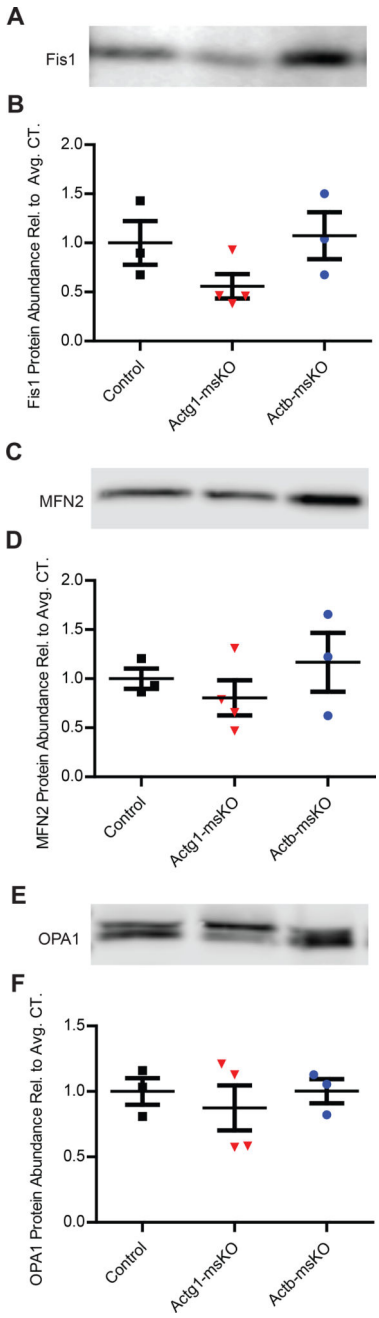

Figure 6. Unaltered abundance of mitochondrial dynamics proteins in isolated mitochondrial from Actg1 and Actb KO skeletal muscles

Western blots and quantification of abundance relative to control average for Fis1 (A–B), MFN2 (C–D), and OPA1 (E–F). 1-way ANOVA with Tukey's post hoc test determined no significant difference.

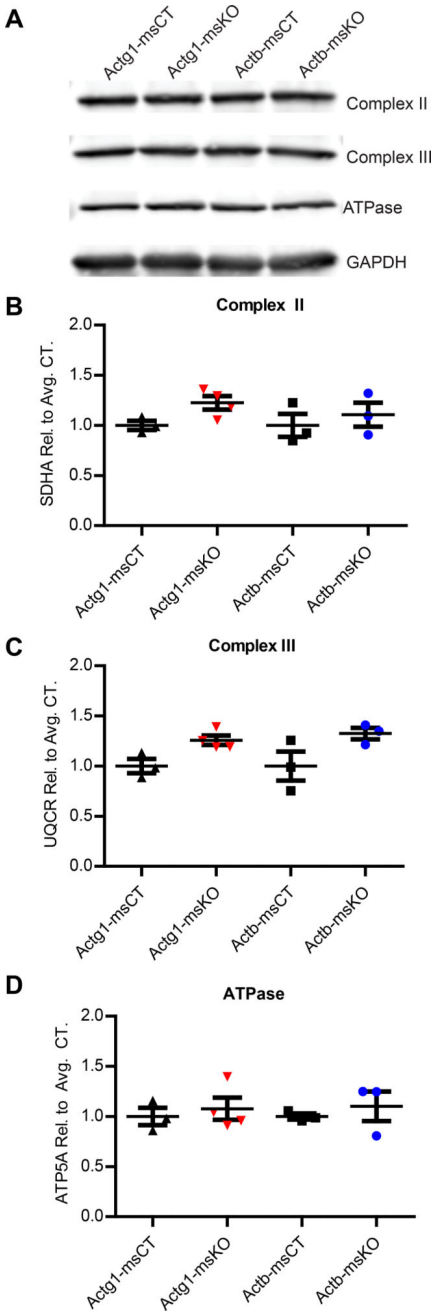

Figure 7. Unaltered abundance of electron transport chain complex proteins in Actg1 and Actb KO skeletal muscle

(A) Representative western blot showing immunoreactivity to proteins from complex II, III, and V. (B) Quantification of SDHA, a complex II protein, immunoreactivity normalized to GAPDH and relative to Actg1-msCT or Actb-msCT mean. (C) Quantification of UQCR, a complex III protein, immunoreactivity normalized to GAPDH and relative to Actg1-msCT or Actb-msCT mean. (D) Quantification of ATP5A, a complex V protein, immunoreactivity normalized to GAPDH and relative to Actg1-msCT or Actb-msCT mean. 1-way ANOVA with Tukey's post hoc test determined no significant difference.

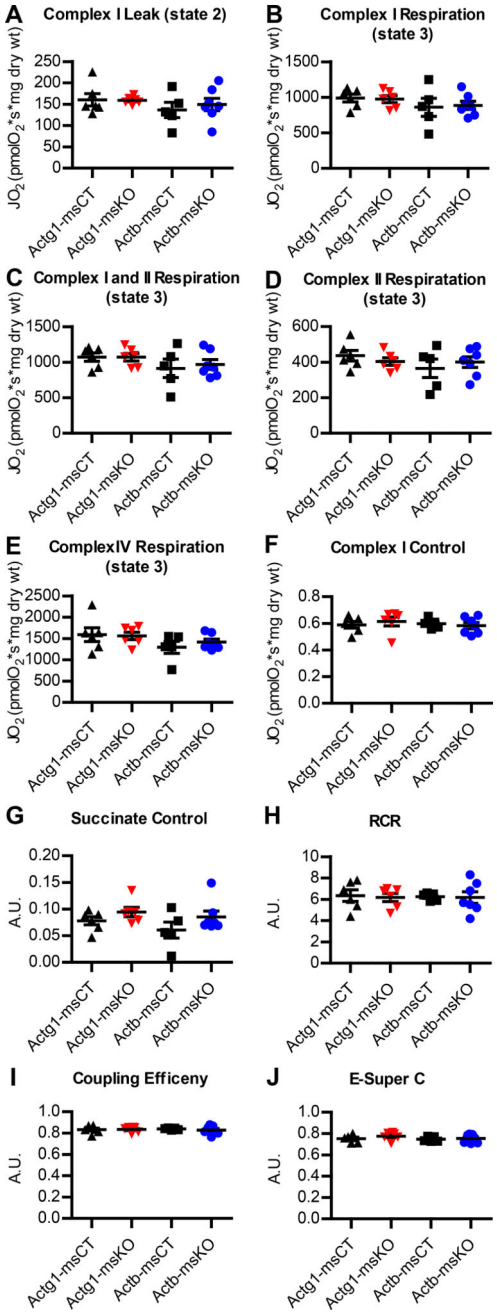

Figure 8. Mitochondrial function is unaffected in Actg1 and Actb KO skeletal muscle

(A–J) Oxygen consumption parameters measured in isolated gastrocnemius fibers. (A) Complex I leak (CI leak), JO_2 was measured in the presence of pyruvate, malate, and glutamate (state 2). (B) Complex I respiration rate (CI), JO_2 was measured in the presence of ADP (state 3). (C) Complex I+II respiration rate (CI+II), JO_2 was measured in the presence of succinate. (D) Complex II respiration rate (CII), JO_2 was measured in the presence of rotenone. (E) Complex IV respiration rate, JO_2 was measured in the presence of antimycin A, ascorbic acid, and TMPD. (F) Complex I control is the ratio of (JO_2 Complex I+II - JO_2 Complex II)/JO_2 Complex I+II. (G) Succinate Control (JO_2 CI+II-JO_2 CI)/JO_2 CI+II. (H)

RCR is the respiratory control ratio it is the ratio of JO_2 CI/JO_2 CI leak. (I) Biochemical coupling efficiency is the ratio of (JO_2 CI - JO_2 CI leak)/JO_2 CI. (J) E- supercomplex is the ratio of JO_2 CI+II/ (JO_2 CI + JO_2 CII). 1-way ANOVA with Tukey's post hoc test determined no significant difference.

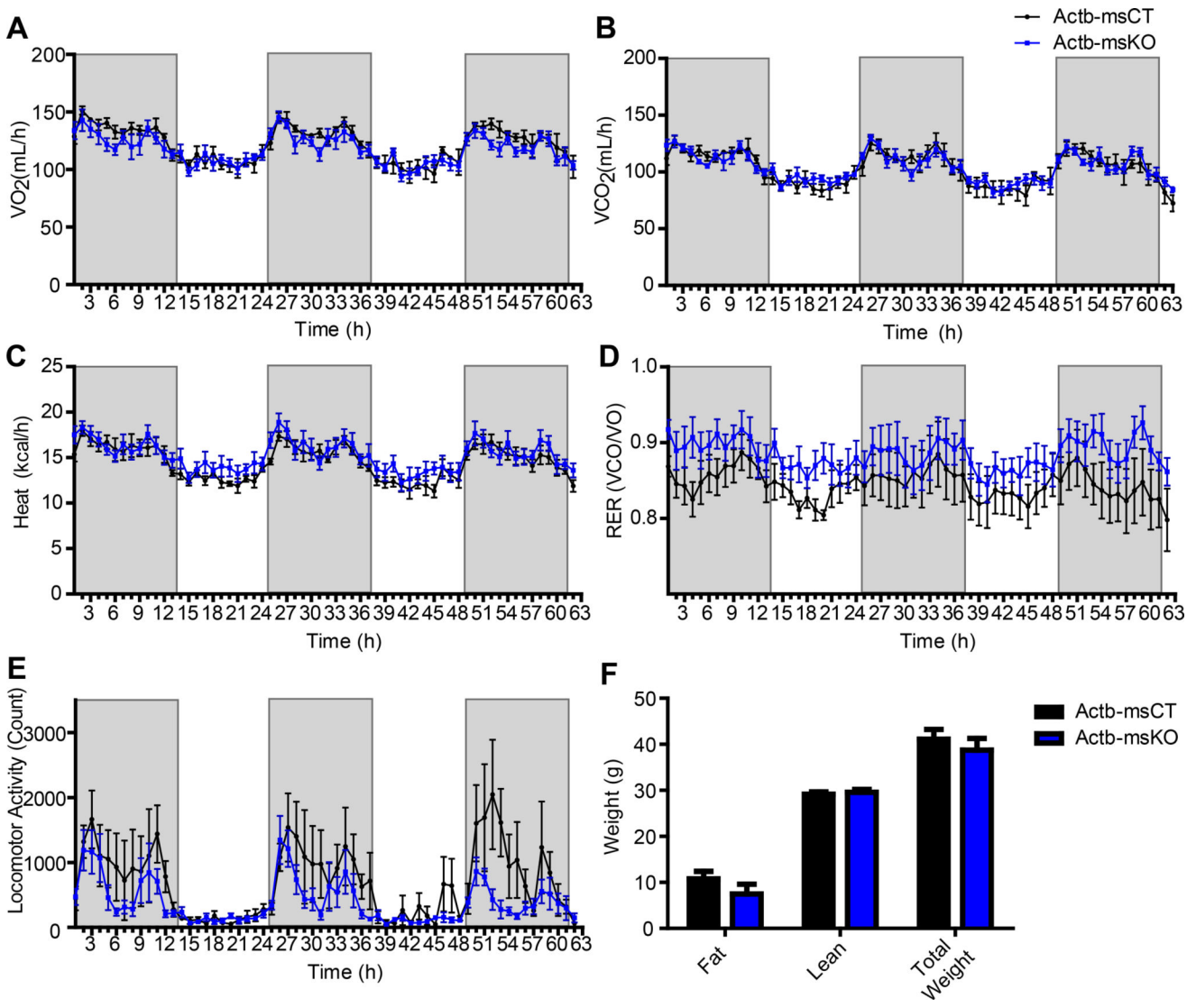

Figure 9. Unaffected whole body respiration in 22–25 month old muscle-specific Actb KO mice

(A–E) Whole body mitochondrial respirometry of 22–25 month old mice. (A) O_2 consumption. (B) CO_2 consumption. (C) Heat released. (D) Respiratory exchange ratio of O_2 to CO_2. (E) Ambulation. (F) Body composition of mice used in study.

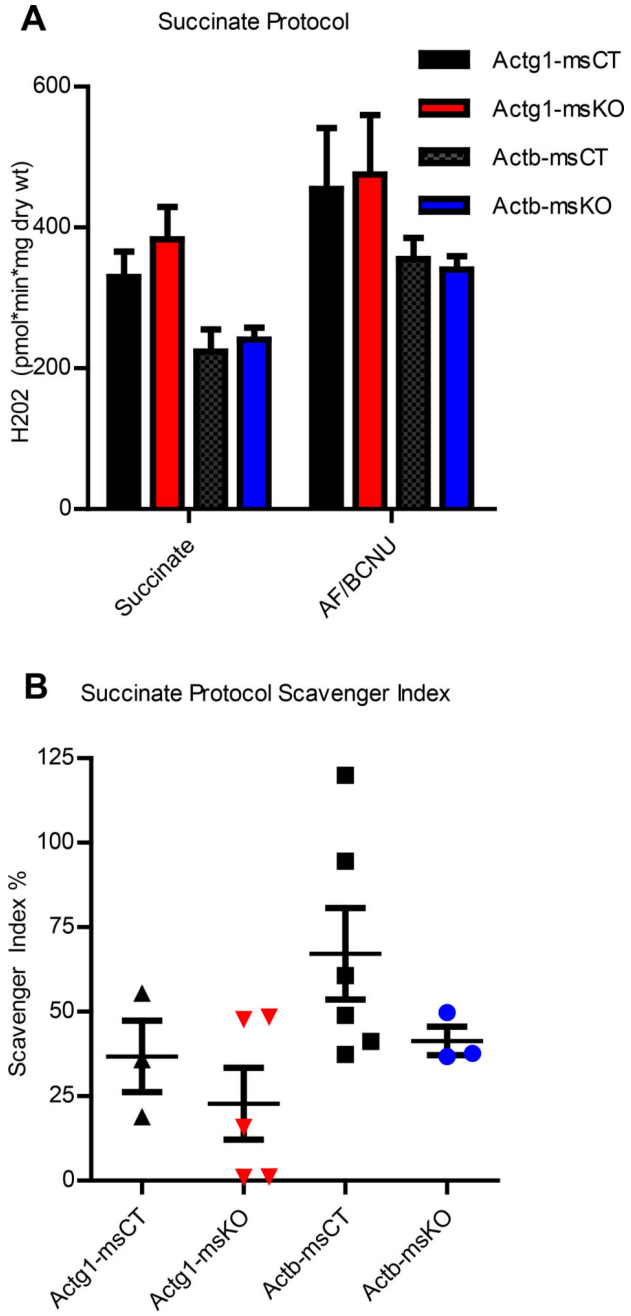

Figure 10. Unaltered H_2O_2 Production in Actg1 and Actb KO skeletal muscle

(A) Succinate stimulated H_2O_2 production in 12 month old animals in the absence or presence (AF/BCNU) of thioredoxin reductase inhibitor AF (auranofin) and glutathione reductase inhibitor BCNU (Carmustine). (B) The scavenger index is the percent increase in succinate induced H_2O_2 production relative to H_2O_2 production when inhibitors are present.

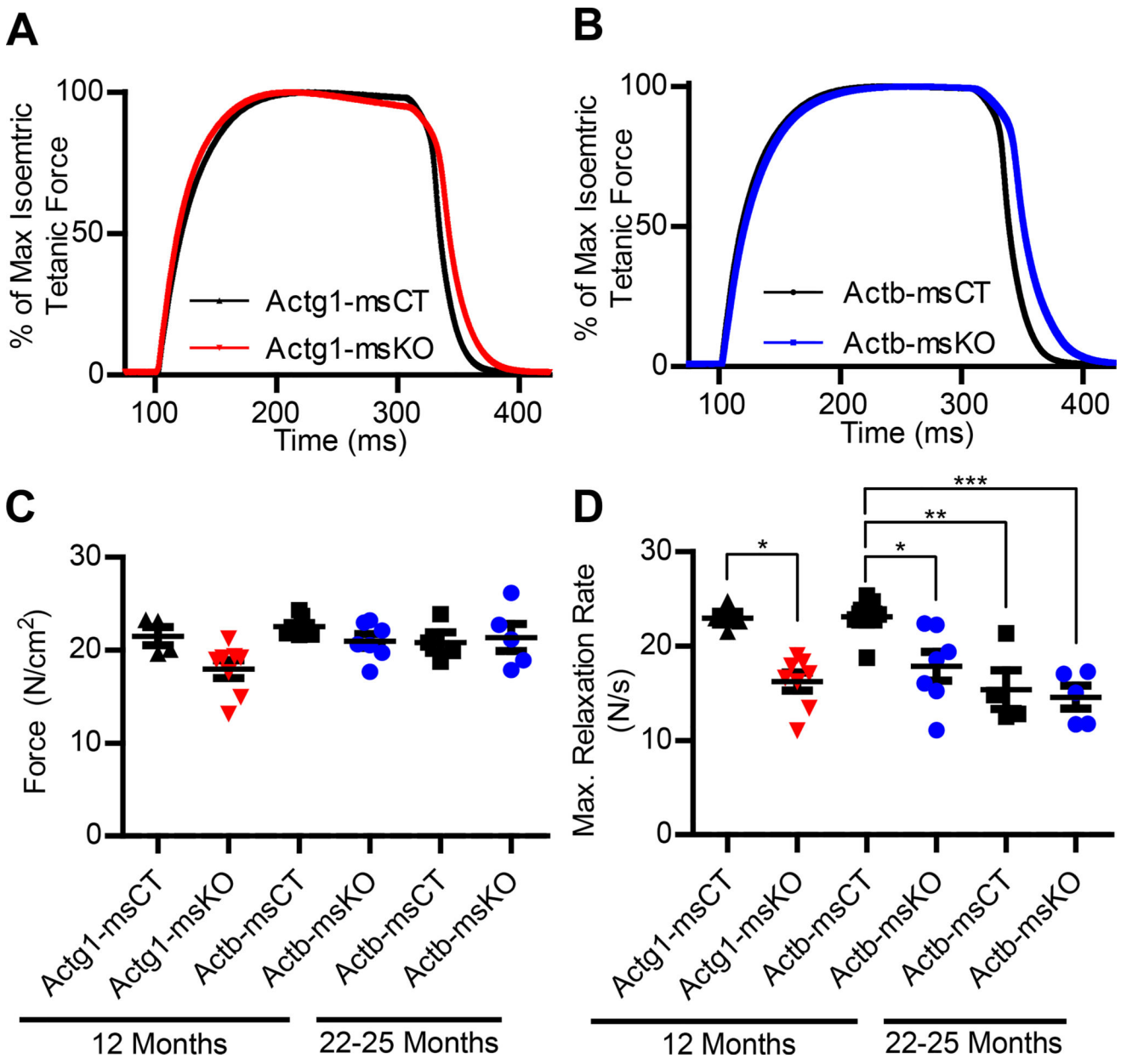

Figure 11. Impaired relaxation rates in Actg1 and Actb KO skeletal muscle

(A–B) Representative isometric contraction force tracings of tetanically-stimulated 12 month old control, Actg1-msKO (A), and Actb-msKO (B) EDL muscles. (C) Peak specific forces generated during maximal isometric tetanic contractions. (D) Maximal rates of relaxation. 1-way ANOVA with Tukey's post hoc test were performed to determine significance. # or * is $0.01<p<0.05$, ** is $0.01<p<0.001$, and *** is $p<0.001$. Error bars are S.E.M.

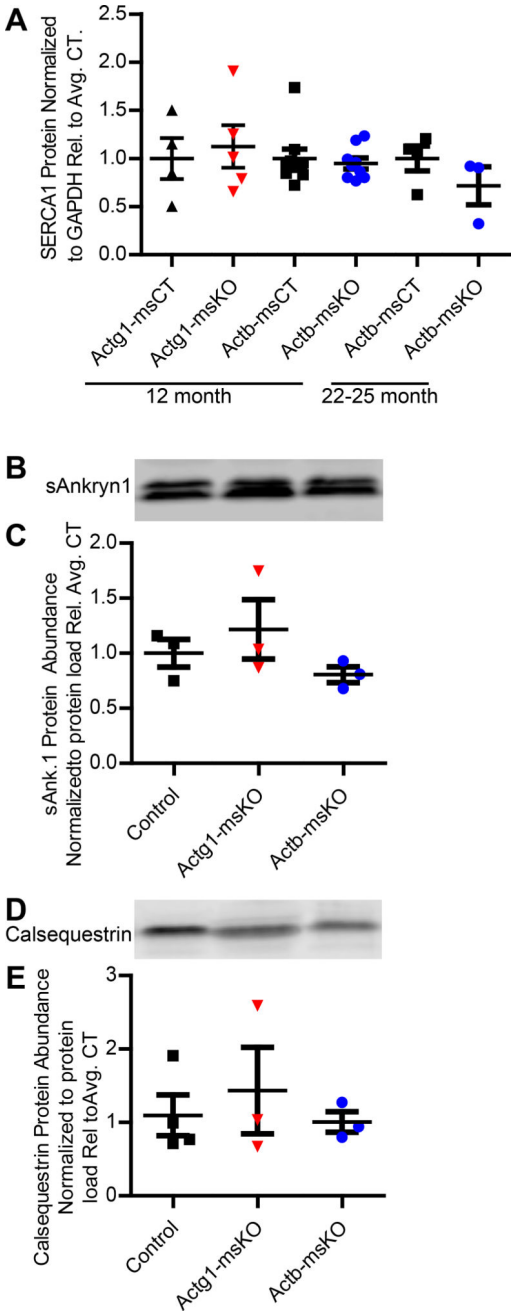

Figure 12. Unaltered SERCA 1 and SR protein abundance in Actg1 and Actb KO skeletal muscle

(A) Quantification of SERCA 1 immunoreactivity normalized to GAPDH relative to control average. (B) Small Ankyrin 1 representative western blot on SR fractions isolated from skeletal muscle. (C) Quantification of small ankryin 1 protein by western blot, normalized to protein load, relative to control average. (D) Calsequestrin representative western blot on SR fractions isolated from skeletal muscle. (E) Quantification of calsequestrin protein by western blot, normalized to protein load, relative to control average. 1-way ANOVA with Tukey's post hoc test determined no significant difference.

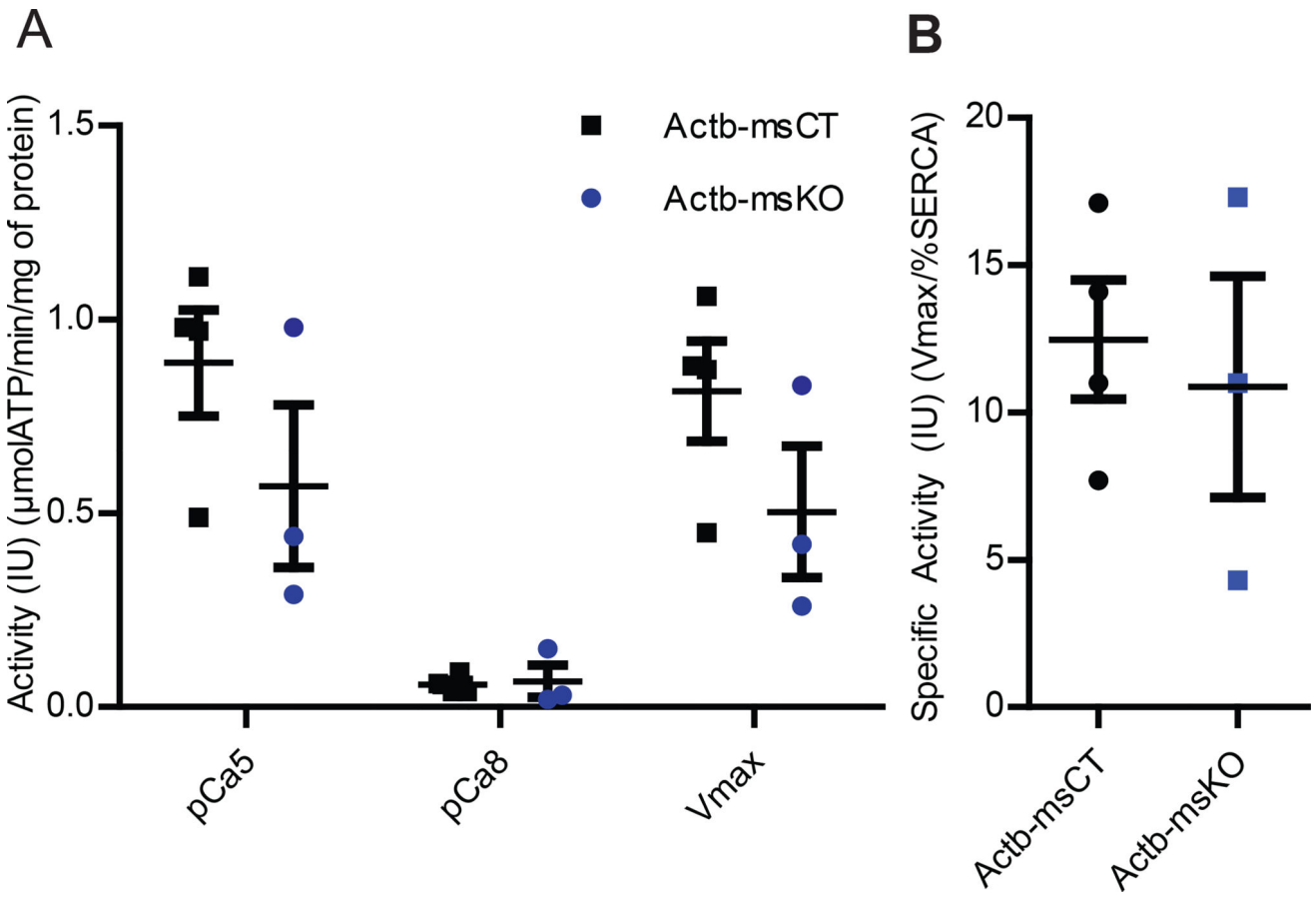

Figure 13. Unaffected SERCA ATPase Activity in SR from Actg1 and Actb KO skeletal muscle

Activity of SERCA (A) Actb-msKO in high (pCa5) calcium, low (pCa8) calcium and Vmax (pCa5-pCa8). SERCA activity relative to SERCA abundance as measured by western blot for (B) Actb-msKO. 1-way ANOVA with Tukey's post hoc test determined no significant difference.

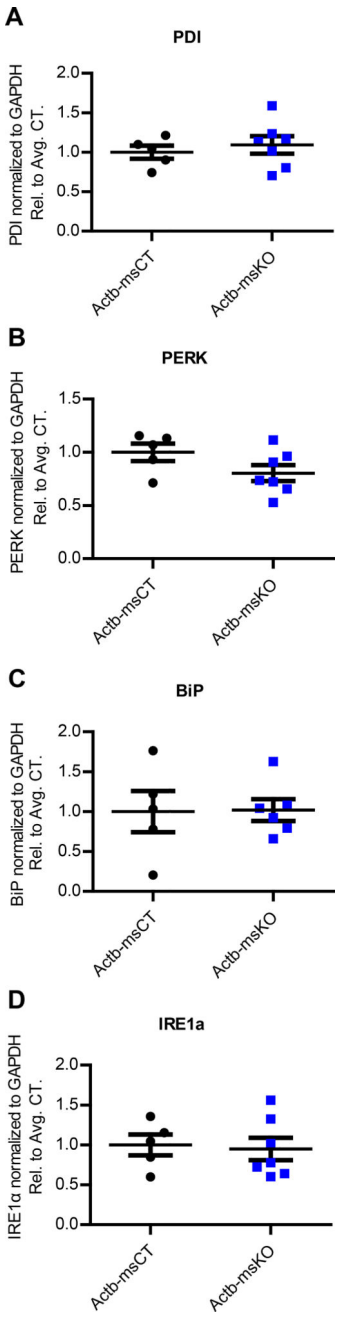

Figure 14. ER Stress Response Pathway Proteins are not upregulated in muscle-specific Actb KO mice at 12 months old

Western blot showing immunoreactivity to ER stress pathway proteins. Quantification of immunoreactivity to PDI (A), BiP (B), PERK (C), and IRE1α (D). All samples were normalized to GAPDH and relative to Actg1-msCT or Actb-msCT mean. 1-way ANOVA with Tukey's post hoc test determined no significant difference.

Table 1

Tetanic isometric contraction measurements in control, Actg1-msKO, and Actb-msKO EDL muscles.

Age	12mo				22–25 mo	
Genotype	**Actg1-msCT**	**Actg1-msKO**	**Actb-msCT**	**Actb-msKO**	**Actb-msCT**	**Actb-msKO**
Maximal Tetanic Force (mN)	491.3 ±11.3	407.5 ±17.2	490.6 ±8.8	442.8 ±21.6	413.8 ±31.3	420.5 ±22.4
Specific Force (N/cm2)	21.5 ±1.0	18.0 ±0.9	22.5 ±0.4	21.0 ±0.7	20.8 ±1.1	21.4 ±1.5
Maximal Contraction Rate (N/s)	17.0 ±1.0	13.7 ±0.5	15.8 ±0.7	14.9 ±0.7	15.1 ±0.6	14.6 ±0.8
Maximal Relaxation Rate (N/s)	23.0 ±0.7	16.2 ±1.0$^{\#}$	23.1 ±0.8	17.9 ±1.5*	15.4 ±2.1**	14.6 ±1.2***
1/2 Relaxation Time (ms)	86 ±12	113 ±3$^{\#}$	87 ±6	100 ±8	86 ± 7	86 ±8
Force Development Time (ms)	149.0 ±13	120 ±4	144 ±6	144 ±8	157 ±8	165 ±10
Fatigue (% of initial maximal tetanic isometric force)	60.8 ±2.3	64.7 ±2.1	60.8 ±2.3	64.7 ±1.8	58.3 ±2.7	64.6 ±2.5
Maximal Force Recovery after Fatigue (% of initial max. tetanic iso. force)	93.0 ±2.1	90.8 ±4.1	93.7 ±1.4	92.5 ±1.8	91.5 ±2.7	95.7 ±2.4

$^{\#}$Denotes comparison to Actg1-msCT.

*Denotes comparison to 12 month old Actb-msCT. 1-way ANOVA with Tukey post-test.

$^{\#}$or * is $0.01<p\leq0.05$,

** is $0.01<p<0.001$,

*** is $p\leq0.001$.